TECHNISCHE UNIVERSITÄT MÜNCHEN

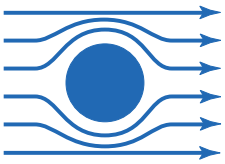

WALTHER-MEISSNER INSTITUT FÜR TIEF-TEMPERATURFORSCHUNG

BAYERISCHE AKADEMIE DER WISSENSCHAFTEN

ACOUSTICALLY DRIVEN SPIN WAVE RESONANCE

Master´s thesis

Adrián Gómez Pardo

Supervisor: Prof. Dr. Rudolf Gross
Advisor: Dr. Mathias Weiler

Garching, December 2019

Fakultät für Physik
Technische Universität München

Contents

1 Introduction

In 1865 J.C. Maxwell presented a set of equations which could entirely describe the electromagnetic field, achieving one of the major milestones in the history of science [1]. After this important contribution, in 1879, Thomas Alba Edison presented the incandescent light bulb, bringing electric light to the people and revolutionizing their lifestyle forever. Later on, in 1882, Nikola Tesla fabricated the first engine to generate alternate current [2], improving the results obtained by Edison, and opening the doors to the technological revolution coming in the 20^{th}-century. All these contributions developed the technology based on the electron´s charge, which led to the understanding and description of the electron with the birth of the quantum theory.

In 1947 J. Bardeen, W. H. Brattain and W. B. Shockley invented the transistor [3], the key element in the modern integrated circuits technology. They were awarded with the Nobel prize in 1957. In 1965, G. E. Moore predicted the size of the transistor to be reduced twice every two years [4]. However, this exponential downsizing is almost reaching its physical limits [5] due to Joule heating and the appearance of quantum-mechanic effects, such as tunneling hinder.

The electron's spin, discovered already in 1922 by Stern and Gerlach [6], provides an additional degree of freedom, which is not explotied in semiconducting transistors. The field of spin electronics or spintronics is concerned with exploiting the intrinsic spin of the electron and its associated magnetic moment, in addition to its electronic charge in solid state devices [7]. Prominent applications in this field are the Giant Magneto Resistance (GMR) and the Tunneling MagnetoResistance (TMR). The generation of spin currents -directed transport of angular momentum [8]- is, crucial for the development of spintronic devices. Spin currents can be transported by electrons or collective magnetic excitation, called spinwaves. In this thesis, our aim has been to study how can we excite spin waves, by coherent phonons, using the so-called Acoustically Driven Ferromagnetic Resonance (ADFMR) [9, 10, 11]. We study ADFMR in a FerroMagnetic (FM)/piezoelectric bilayer, where the strain in the piezoelectric material is induced by Interdigital Transducers (IDTs). We use $Co_{25}Fe_{75}$ (CoFe) as the FM layer. In this metallic, magnetoelastic [12] ferromagnet, a spin-wave decay length of up tp 20 µm has been observed [13].

In previous works, ADFMR has been studied in detail using different ferromagnetic materials such as Ni or Co [14, 10, 9, 11]. The choice of CoFe in the present work is based on the outstanding properties presented by this material such as its low damping comparable to the damping of insulating FM, and its high magnetization saturation [15]. These properties make this material a promising candidate for novel spintronic devices. Different techniques have been used during our thesis, including microwave spectroscopy to characterize the magnon-phonon coupling at frequencies up to several GHz, and Brillouin Light Scattering (BLS) to optically detect magnon-phonon interaction. Furthermore, the Frequency-Resolved Magneto Optic Kerr Effect (FRMOKE) has been employed to optically detect travelling magneto-acoustic waves in the CoFe structures.

2 Theory

In this section we introduce the theoretical concepts of critical importance within this thesis. First, ferromagnetic resonance (FMR) is presented. This physical concept is widely known and its understanding is crucial in the development of this thesis. Second, the concept of surface acoustic waves and how are they generated is presented. In particular Rayleigh waves are introduced, While, these two concepts initially seem to be separated from each other, their mutual interaction via the magnetoelastic coupling [11, 16, 17], is the cornerstone of this thesis.

2.1 Ferromagnetic Resonance

A ferromagnet has a spontaneous magnetization even in the absence of an applied magnetic field. A magnetic moment points along a single direction [18], causing a macroscopic net magnetization **M**. One can control the direction of the net magnetization by applying, e.g., an external magnetic field $\mathbf{H}_0$. In real samples, also anisotropies and demagnetization fields have to be taken into account. Thus the direction of **M** is controlled by the effective field given by

$$\mathbf{H}_{\text{eff}} = \mathbf{H}_0 + \mathbf{H}_{\text{aniso}} - \mathbf{H}_{\text{demag}}, \tag{2.1}$$

where $\mathrm{H}_{\text{aniso}}$ is the anisotropy field contribution and $\mathrm{H}_{\text{demag}}$ is the demagnetization field or stray field present in the sample, this term is represent as a negative due to its tendancy to reduce the total magnetic moment. In thermal equilibrium the magnetization is pointing in the direction of $\mathbf{H}_{\text{eff}}$. If we perturb the system, e.g., by forcing $\mathbf{H}_{\text{eff}}$ to enclose an angle θ with respect **M,** a precession of **M** along $\mathbf{H}_{\text{eff}}$ will start, as is shown in Fig. 2.1.a) This precessional motion will, after a short time, come to an end due to damping effects [19]. This situation is well described by the so-called Landau-Lifshitz-Gilbert equation (LLG)

$$\frac{\partial \mathbf{m}}{\partial t} = -\gamma \mathbf{m} \times \mu_0 \mathbf{H}_{\text{eff}} + \alpha \mathbf{m} \times \frac{\partial \mathbf{m}}{\partial t}, \tag{2.2}$$

where the first term on the right side represents the precessional motion of the magnetization around $\mathbf{H}_{\text{eff}}$ [20] and $\mathbf{m} = \mathbf{M}/\mathrm{M}_s$ with M_s being the saturation magnetization in a macrospin model. Furthermore, γ and μ_0 are the gyromagnetic ratio and vacuum permeability respectively. The resulting precession frequency of **M** around H_{eff} as exemplarily shown in Fig. 2.1.c) is given by

$$\omega = \gamma \mu_0 |\mathbf{H}_{\text{eff}}|. \tag{2.3}$$

The second term on the right side in Eq. (2.2) describes the damping with the phenomenological damping parameter α, this term was introduced in the in the notation of Eq. (2.2) by T. Gilbert in 2004 [21].

When a driving field $\mathbf{h}_{\text{rf}}(t)$ is applied perpendicular to H_{eff} with the precession frequency, the damping term can be counteracted, and the precession is sustained as long as the driving field $\mathbf{h}_{\text{rf}}(t)$ is applied, as schematically shown in Fig. 2.1.b) and c) The system is now in Ferromagnetic Resonance (FMR).

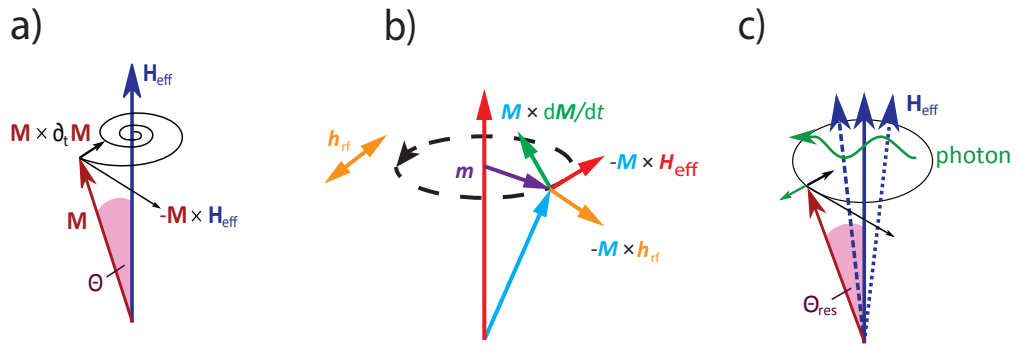

Figure 2.1: a) First term in the right side of Eq.(2.2), in this situation the magnetization **M** will relax along **H.** b) Schematic for FMR, all the terms described in Eq.(2.2) are represented, this image is taken from [22]. c) The FMR is driven by a source of coherent photons. Images a) and c) are taken from [14]

Typically, for experimentally accesible magnetic fields this precessional frequency lies in the GHz regime. In conventional FMR studies the driving field is provided by microwave photons. However, due to magnetoelasticity, strain within a ferromagnet induces a virtual driving field [11, 10], enabling acoustically driven FMR (ADFMR).

2.2 Surface Acoustic Waves and their Generation

SAWs are elastic waves propagating at the surface of a solid. They were first described by Lord Rayleigh in 1885 [23]. A schematic depiction of a SAW can be seen in Fig. 2.2

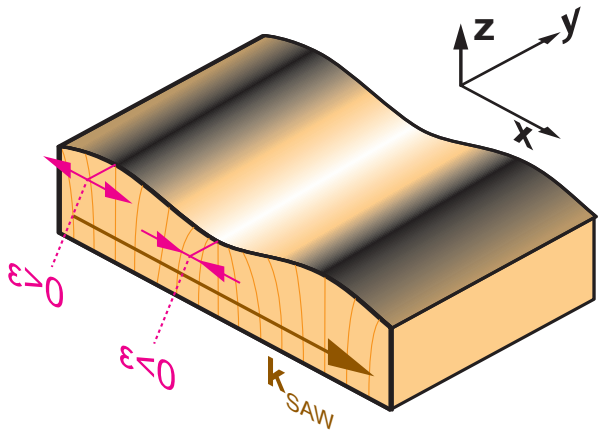

Figure 2.2: Schematic illustration of a SAW. The SAW generates regions with compressive strain ($\varepsilon < 0$) and dilative strain ($\varepsilon > 0$) on the surface of a solid. Image taken from [9]

An elastic wave can either be compressional or shear type. Any combination of both is also possible. SAWs devices with frequencies in the GHz regime are of fundamental importance in numerous communications and electronics devices [24] and are well established [25].

In this thesis we focus on one particular type of SAW, which is known as Rayleigh wave. SAWs can be described in terms of their strain components ϵ_{ij} where $i, j \epsilon \{1, 2, 3\}$ are indices indicating the three spatial directions in a cartesian reference frame. In general, any Rayleigh wave propagating in one direction consist of a compressional wave with a wave-vector $\mathbf{K}$ parallel to the displacement$\mathbf{,u}$,in that direction, a shear horizontal wave with a wave-vector $\mathbf{K}$ perpendicular to the propagation direction, and a shear wave also vertical to the propagation direction as despicted in Fig. 2.3.

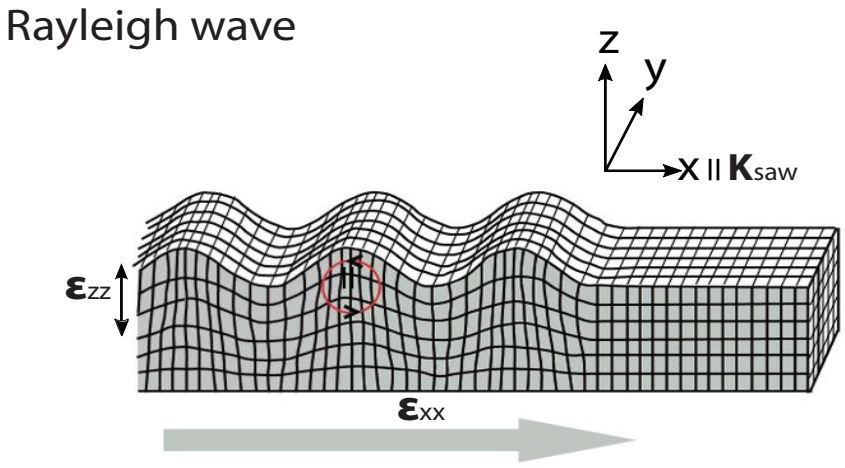

Figure 2.3: Rayleigh wave with compressional components in x parallel to the displacement and z perpendicular to the displacement and a shear vertical component in the xz-plane

In this thesis, we are interested in the propagation of Rayleigh waves at the interface of a piezoelectric material, $LiNbO_3$ (LNO) [26], where a SAW can be generated or detected, and a ferromagnetic material, $Co_{25}Fe_{75}$ (CoFe), supporting spin-waves. A remarkable property of Rayleigh waves is the 90^o phase shift between the longitudinal and the transversal dispacements. A deeper mathematical description can be found in [27, 28]. Typical SAW velocities on LNO are around 3500 m/s for frequencies of 1 GHz [23, 14] and therefore $\lambda_{\mathrm{SAW}} = 4\,\mu$m, which is a really accesible lenght scale for either optical lithography or electron beam lithography. For generation and detection of SAWs we introduced the concept of interdigital transducer (IDT).

Typically SAW devices are fabricated onto a piezoelectric material to which a periodic comb-shaped IDT pattern is developed. The shape and arrangement of the IDT electrodes, which we henceforth call fingers, determines the wavelength of the acoustic wave. A detailed list of all the parameters involved and how they affect the SAW can be found in [14]. When an ac current is applied to one of the IDTs, the acoustic wave is generated and travels through the sample (LNO) surface until it arrives to a second IDT in which the acoustic signal is transformed into an electrical signal via the inverse piezoelectric effect as schematically depicted in Fig.2.4.a). Such device consisting of two opposing IDTs that allows for interconversion of electrical and acoustical signals is called delay line. Fig. 2.4.b) shows a micrograph of a corresponding device fabricated during this thesis. The delay line in Fig. 2.4.b) has been loaded with a rectangular (dark grey) ferromagnetic thin film.

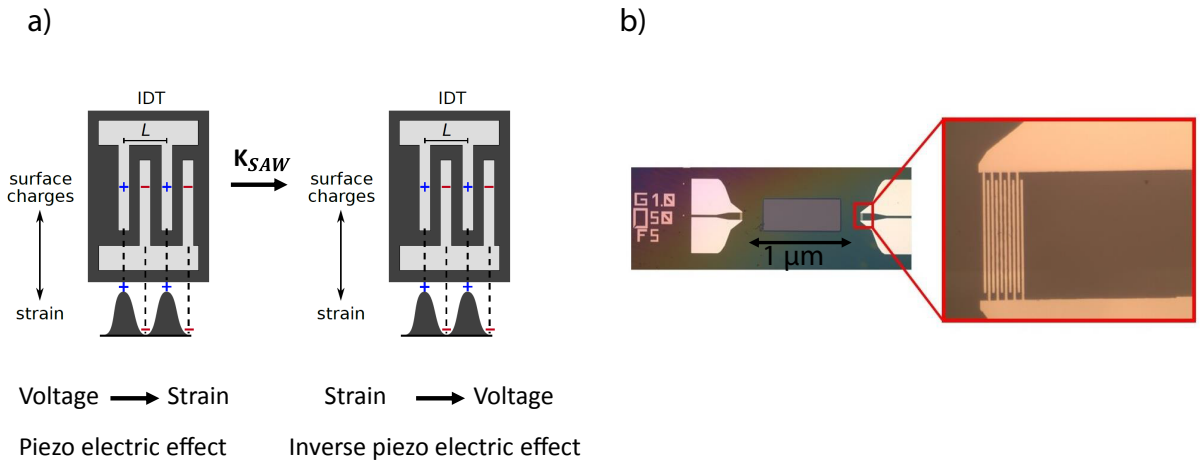

Figure 2.4: a) Schematic view of an IDT delay line showing how the IDTs transform the applied voltage into strain and vice-versa. b) Optical microscope image of a delay line fabricated during this thesis.

2.3 Magnetoelastic Coupling

In this section, we described how coherent phonons can be used to drive magnetization dynamics.

in section. 2.1 we introduced the concept of $\mathbf{h}_{\mathrm{rf}}(t)$ as the driving field that one should apply perpendicular to the system to drive the magnetization dynamics. This driving field is commonly obtained from a microwave photons source. It is also well established that not only photons but also phonons can be used to drive FMR [11, 17, 16, 28, 14, 9], which we explain in the following.

The following derivation follows Refs.[11, 9]. Phonon-magnon coupling arises from the fact that in most ferromagnetic media, lattice distortion described by a strain tensor $\hat{\epsilon}$ is directly linked to magnetic anisotropy. This is widely studied [18] and is known by magnetoeslasticity or inverse magnetostriction [29].

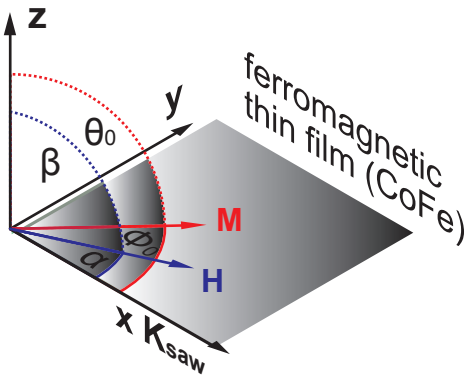

Figure 2.5: Cartesian reference frame $\{\mathrm{X}, \mathrm{Y}, \mathrm{Z}\}$ referred to the ferromagnetic thin film. **M** and **H** are in the ferromagnetic thin film plane. This image is adapted from [9]

For simplicity and without loss of generality we consider just pure strains in the following, thus, no shear components are present and only diagonal elements of $\hat{\epsilon}$ are taken into account, resulting in the strain tensor

$$\hat{\epsilon} = \begin{pmatrix} \epsilon_{xx} & 0 & 0 \\ 0 & \epsilon_{yy} & 0 \\ 0 & 0 & \epsilon_{zz} \end{pmatrix}. \tag{2.4}$$

Now we considered only a SAW propagating along the x direction and strain in the direction of propagation, as we have introduced in Sec. 2.2, $\mathbf{u}_x$, so that $\mathbf{u}_y = \mathbf{u}_z = 0$. It is extremly useful to introduce a new reference frame $\{\mathrm{x}_1, \mathrm{x}_2, \mathrm{x}_3\}$ in which x_3 points in equlibrium **M**-direction as depicted in Fig. 2.6

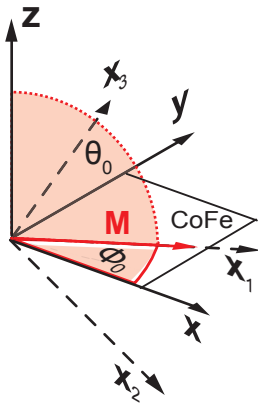

Figure 2.6: New coordinate system $\{x_1, x_2, x_3\}$ in which x_1 is pointing in the same direction of **M,** x_2 is in the film plane.

The link between the laboratory reference frame X, Y, Z and the new coordinate system $\{x_1, x_2, x_3\}$ is given by

$$\begin{pmatrix} x \\ y \\ z \end{pmatrix} = \tilde{R} \begin{pmatrix} x_1 \\ x_2 \\ x_3 \end{pmatrix}, \tag{2.5}$$

where $\tilde{R}$ is defined by

$$\tilde{R} = \begin{pmatrix} \cos\theta_0 & -\sin\theta_0 & 0 \\ \cos\phi_0\sin\theta_0 & \cos\phi_0\cos\theta_0 & -\sin\phi_0 \\ \sin\phi_0\cos\theta_0 & \sin\phi_0\cos\theta_0 & \cos\theta_0 \end{pmatrix}, \tag{2.6}$$

and $\{\theta_0, \phi_0\}$ are the angles that define the equilibrium direction of **M** in Fig. 2.5. In this new reference frame, the magnetoelastic AC contribution to the anisotropy field is given by [30]

$$F^{AC}(t) = B_1 \epsilon_x(t) m_x^2, \tag{2.7}$$

where $m_x = m_x(\phi_0, \theta_0)$ is given by

$$m_x = m_1\cos\theta_0 - m_2\sin\phi_0, \tag{2.8}$$

and B_1 is the magnetoeslastic coupling constant. From this argument and from the selected geometry of the situation, the driving AC field for ADFMR is given by

$$\mu_0 \mathbf{h}_{magel}(t) = -\nabla_{m_1 m_2} F^{AC}(t). \tag{2.9}$$

We can add now $\mathbf{h}_{magel}(t)$ as a contribution of $\mathbf{H}_{eff}$ in Eq. (2.1). Now the LLG equation

can be solved analogously as we showed in previous section. It is clear that $\mathbf{h}_{\text{magel}}$ is a function of $\mathbf{M}$ orientation and the strain tensor $\tilde{\epsilon}$.

3 Experimental Techniques

In this chapter we present the experimental techniques used whitin this thesis. First we introduced the concept of a Vector Network Analyzer (VNA), its principles and which information can be extracted in a VNA measurement. Second, the microfocused Frequency Resolved Magneto-Optical Kerr Effect (FRMOKE) setup used for measurements is disscused. The last part of this chapter introduces the basic physics of the Brillouin Light Scattering (BLS) technique and presents the microfocused BLS setup.

3.1 Vector Network Analysis

A VNA is one of most common instrument used to characterize circuits in Radio Frequency engineering. Employing a VNA we are able to determine amplitude and phase information [31] from measurements on a delay lines formed by two IDTs, as shown in Fig. 2.4.b, We are interested in the so-called wave quantities and scattering parameters (S-parameters). One can distinguish between incident wave $a(t) = A\sin(\varphi_1 t)$, and a reflected wave $b(t) = B\sin(\varphi_2 t)$, as schematically shown in Fig. 3.1.

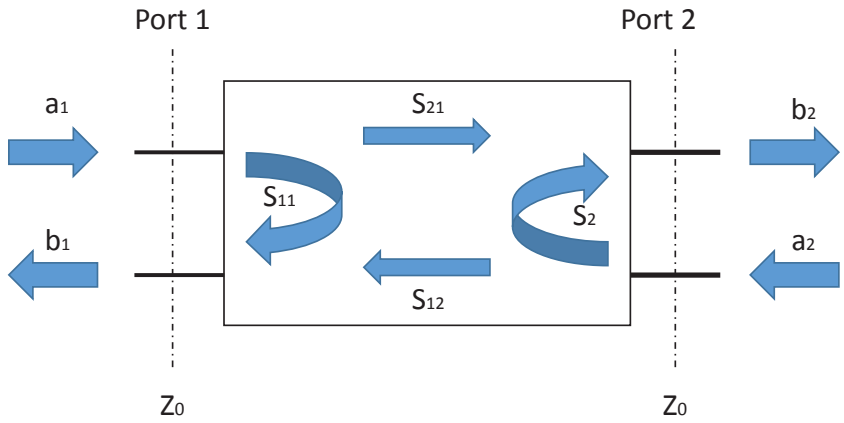

Figure 3.1: Schematic drawing of a two-port device with waves quantities and S-parameters.

The Scattering parameters (S-parameters) are defined as the ratios of the respective wave quantities.

$$\begin{pmatrix} b_1 \\ b_2 \end{pmatrix} = \begin{pmatrix} S_{11} & S_{12} \\ S_{21} & S_{22} \end{pmatrix} \begin{pmatrix} a_1 \\ a_2 \end{pmatrix} \tag{3.1}$$

The reflection coefficient is given by

$$\Gamma = b/a, \tag{3.2}$$

which is in general a complex value.

In general, a VNA generates an oscillatory test signal that travels through the device under test (DUT) and measures the reflected and transmitted signals at the same frequency. In our case the DUT is a delay line formed by two IDTs with a ferromagnet in the middle. The VNA measures the response of the DUT. As shown in Fig. 3.2 for a transmission measurement, the VNA is thereby sensitive to amplitude ratio and phase difference of the involved waves a_1 and b_2.

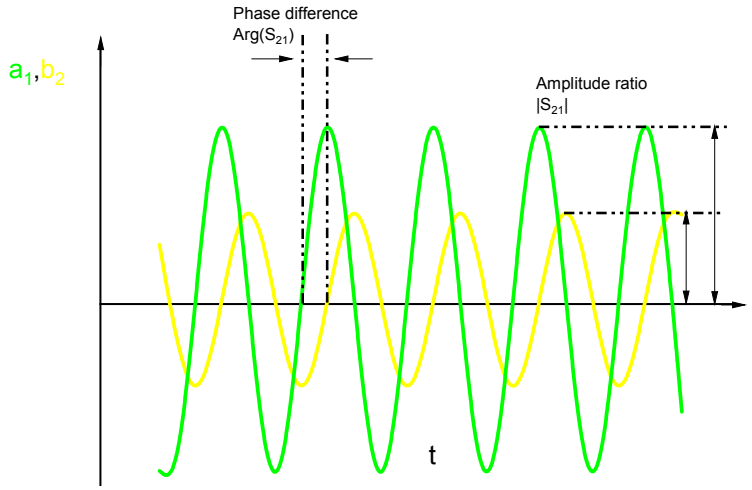

Figure 3.2: a_1 and b_2 are shown, being the applied stimulus and the response measured by the VNA, respectively.

In this thesis we represent the amplitude ratio $|S_{21}|$ in a logarthmic scale, using the following expression

$$|\mathrm{S}_{21}|\,(\mathrm{dB}) = 20\cdot \log_{10}|\mathrm{S}_{21}| \tag{3.3}$$

In this thesis we used VNA models ROHDE & SCHWARZ ZVA 24 GHz (2 port) or AGILENT PNA-X 26.5 GHz (4 port) depending on availability.

3.2 Fourier Transformation

In our VNA measurements, we determine the transmission S_{21} through our SAW dely lines as a function of the frequency. Typical frequency dependent data (FD) is shown in Fig. 3.3.a). Spurious noise such e.g., higher transit are masking the SAW signal we are interested in. Fortunately this issue can be solved by, applying an Inverse Fourier Transformation (IFT) to our FD obtained data, thus obtaining Time Dependent data (TD). Once the EMC is removed from our TD data, we apply a Fourier Transformation (FT) to our TD data. Now we have FD data without any spurious signals, so that, only the SAW signal is present.

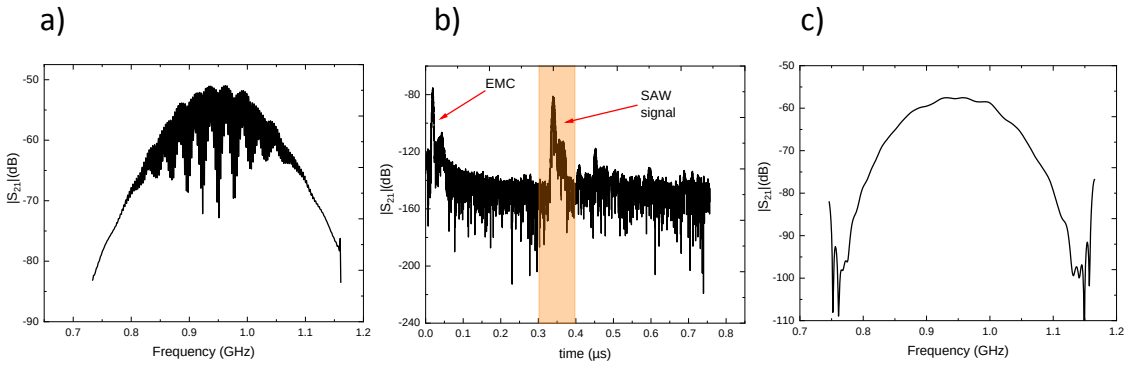

Figure 3.3: a) Raw data for a measurement performed with one of our sample. The central frequency for the first harmonic is at 0.93 GHz. b) Time dependet data after IFT. Due to their very different traveling times, the EMC and the SAW signal are perfectly distinguishable from each other. The rectangle time gate is only apply at the SAW signal. c) After rectangle time gate and FT the SAW signal is perfectly visible.The SAW signal mimic a sinc^2 function [9].

In the following we describe the entire algorithm, and we introduce the concept of windowing.

After a VNA measurement is performed, we obtain S_{21} FD data as shown in Fig. 3.3.a) which is mostly formed by the SAW signal, EMC and higher transit signals. In general, we program the VNA to measure over a certain frequency region, which depends on the IDTs design, and with a certain frequency span. The FD data then runs through an algorithm which removes the sporious noise performing an IFT as its major step. The array, which we call $\boldsymbol{C}(f, N)$ with f > 0, in the following, has a certain, finite, number of componets. Of course, all of these componets are the FD data obtained after the measurement. Now we multiply a window function to the array. There are several types of window function, but

in all the measurements done within this thesis we've used the so-called hamming window, given by

$$\mathrm{w(f)} = 0.54 - 0.46 \cdot \cos\left(\frac{2\pi \mathrm{f}}{\mathrm{F}-1}\right) \tag{3.4}$$

and therefore we have

$$\mathbf{C}'(\mathrm{f}) = \mathbf{C}(\mathrm{f}) * \mathrm{w(f)} \tag{3.5}$$

where f is the discrete frequency index and F is the total number of involved frequencies. The reason to used a window function is to avoid the apparence of ringin-artifacts due to Gibbs phenomenon [32]. After the window function is applied to the array, we should add zeroes down to 0 GHz frequency, thus spanding the array. This step is known as zero padding and is a well stablished step and vey common in signal processing [33]. Besides the zero padding step it is also necesary to extend (mirror-step) the array to negative frequencies $\mathbf{C}' \rightarrow \mathbf{C}'^{*}$, this step is crucial to correctly carry out the IFT. The total number of elements in $\mathbf{C}'^{*}$ is 2N-2, where N is the total number of elements in the array, as there are two elements in the array that are not reflected, one is the 0 GHz element and the other one is the one associated to the Nyquist frequency, also known as cut-off frequency [34]. At this point we add more zeroes. Now the array is ready to carry out the IFT

$$\mathbf{C}'^{*}(\mathrm{f}) \rightarrow \mathcal{F}^{-1}\left\{\mathbf{C}'^{*}(\mathrm{f})\right\}(\mathrm{t}) \tag{3.6}$$

Thereafter, we apply a rectangular time gate, meaning, we set all to zero instead the information we are interested in, in our case, the SAW signal, see Fig. 3.3.b) After the rectangular time gate is applied to the array, we carry out the FT to the obtained "clean" frequency data.

$$\mathbf{C}'^{*} = \mathcal{F}\left\{\mathcal{F}^{-1}\left\{\mathbf{C}'^{*}(\mathrm{f})\right\}(\mathrm{t})\right\}(\mathrm{f}) \tag{3.7}$$

Now, we just devide the resulting array by the Hamming window function applied at the beginning, Fig. 3.3.c)

$$\mathbf{C} = \frac{\mathbf{C}'^{*}}{\mathrm{w(f)}} \tag{3.8}$$

For a deeper mathematical description, please, refer to [34].

3.3 Brillouin Light Scattering Spectroscopy

Brillouin Light Scattering (BLS) spectroscopy relies on the inelastic interaction of photons with quasiparticles such as either spin-waves (magnons) or phonons. It was first worked out by L. Brillouin in 1992 [35]. In the following, we introduce the physics and key aspects for this powerful technique.

The BLS process can be explained using a quantum-mechanics picture, where incoming photons provided by a source of coherent photons, in this case a laser beam with a wavelength of $\lambda = 532\,\mathrm{nm}$ with a very small bandwith ($< 10\,\mathrm{MHz}$) undergo scattering with either phonons or magnons with the constrain of the conservation of total energy and linear momentum

$$\hbar \mathrm{f_s} = \hbar \mathrm{f_i} \pm \hbar \mathrm{f_q}, \tag{3.9}$$

$$\hbar \mathrm{k_s} = \hbar \mathrm{k_i} \pm \hbar \mathrm{k_q}. \tag{3.10}$$

Where $\hbar$ is the reduced Planck constant and $\mathrm{f_s}, \mathrm{f_i}, \mathrm{f_q}$ are the frequency of the scattered photon, the frequency of the incident photon and the frequency of the created (annihilated) quasi particle, respectively.During the process, two possible situations can take place. The first possibility is the creation of a quasi-particle, which is known as Stokes process as depicted in Fig. 3.4.a), here the scattered photon has less total energy and linear momentum than before the scattering event. The second possibilty is the inverse situation, in which the annihilation of a quasi-particle happens, the scattered photon has a higher total energy and linear momentum than the incoming photon. This second situation is known as Anti-Stokes process and is depicted in Fig. 3.4.b). At room temperature, both processes occur with roughly the same probability [36].

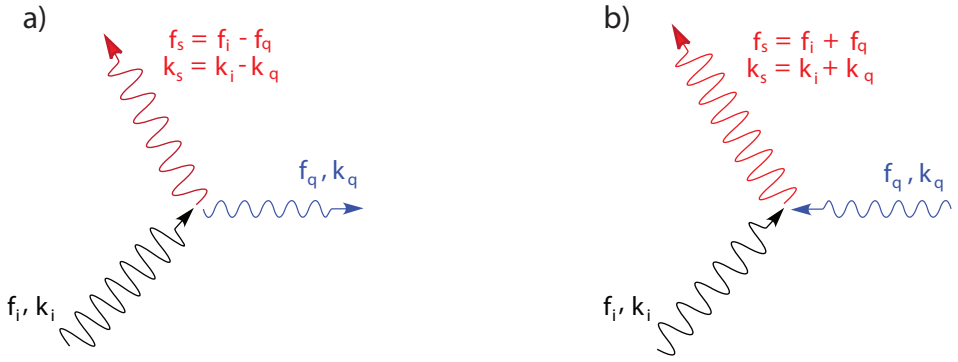

Figure 3.4: a) Creation of a quasi-particle, the scattered photon has reduced total energy and linear momentum compared to the incoming photon. b) Annhilation of a quasi-particle. This image is adapted from [14].

Due to conservation of the angular momentum, the scattered photon after scattering with a magnon undergoes a polarization rotation of $\frac{\pi}{2}$ with respect to its initial polarization,

whereas the scattered photon with a phonon does not obtain any polarization rotation.

Magnons in ferromagnets, have typically GHz frequencies, while the photons coming from the laser light have THz frequencies, thus meaning that the change in frequency for the scattered light compared to the incoming light is really small. This directly implies that a sophisticated measuring tool is needed to be able to detect this tiny amount of change in frequency. To this end we used a so called Tandem Fabry-Perot Interferometer (TFPI). Technical description and a concise mathematical description can be found in [37, 14, 38, 39]. The total experimental setup used in this thesis is presented in Fig. 3.5.

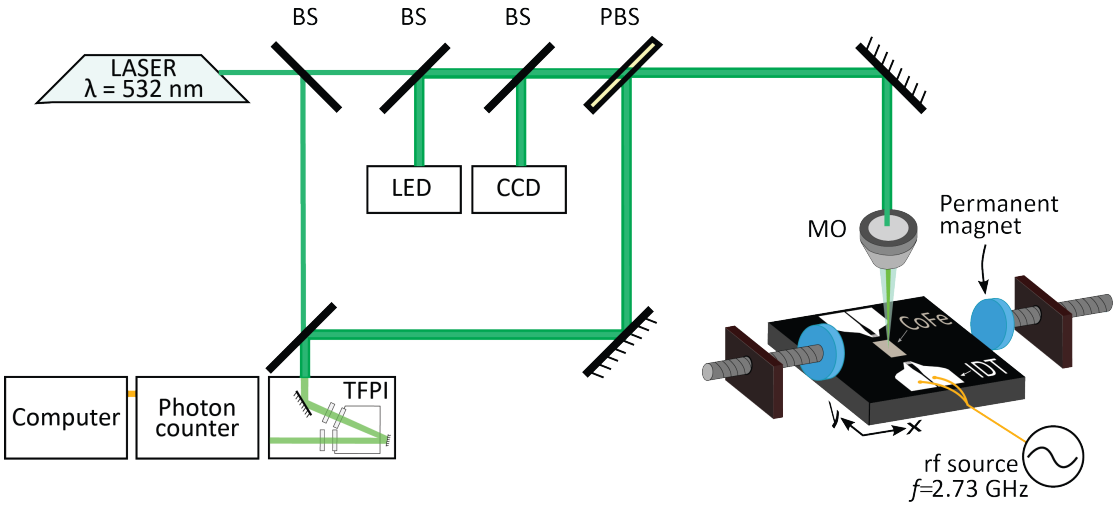

Figure 3.5: The experimental setup for micro BLS is illustrated. This image is adapted from [14].

The laser light is first sent trough a beam splitter that direct part of the beam directly to the TFPI. This part of the beam is used to stabilized the interferometer. The other part of the beam is directed trough a linear Polarizing Beam splitter (PBS), thus the light coming out this polarizer is linearly polarized. This linearly polarized light is focused onto the magnetic sample with the help of a Microscope Objective (MO) with a numerical aperture of N.A = 0.75. This linearly polarized light scatters with either magnons or phonons in the magnetic sample. Two permanet magnets provide an external static magnetic field $\mathbf{H}_{\text{ext}}$. To perfom magnetic field sweps the permanent magnets are connected to a stepper motors that can control the distance between them. The backreflected/ scattered light is directed to the PBS. In the ideal case only light with a $\frac{\pi}{2}$ polarization rotation can pass trough the PBS, thus only light scattered off by magnons, as explained above, is directed to the TFPI. Light scattered off by phonons is strongly supressed. Additionally a source LED light is added into the optical path and recorded by a CCD, thus creating an image of the sample and the laser spot position. The sample is placed on a movable stage controled by piezoelectric motors with a scanning range of 100x100 μm^2. The typical BLS spectrum recorded during a single measurement is showed in Fig. 3.6.b). The highlighted area is the Region Of Interest (ROI) which corresponds to the Stokes peaks, or in other words, corresponds to the creation

of quasi-particles (magnons) after scattering as described in Eqs. (3.9) and (3.10). In this particular case, a SAW with frequency of 2.73 GHz was excited. The central peak is used to stabilize the interferometer and is always centered at 0 GHz.

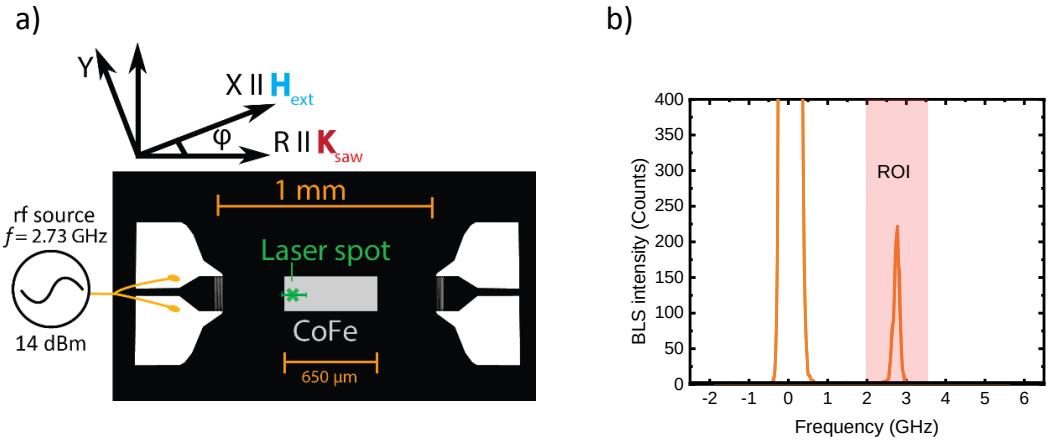

Figure 3.6: a) Laser position on the sample during one measurement, image adapted from [14]. b) Typical recorded BLS spectrum. The region of interest is highlighted

After a Scattering process of photons with magnons, there is an upper limit for the **K** magnitude that can be collected by the MO. This upper limit is restricted by two times the maximun k-vector of the incident light [36], and only the in-plane (IP) wave vector components are conserved, but the Out-Of-Plane (OOP) are not. Mathematically this is expressed in Eq. (3.11)

$$\mathrm{K}_{\mathsf{magnon,max}} = \frac{4\pi}{\lambda n_{\mathsf{env}}} NA \tag{3.11}$$

where λ is the laser wavelenght, here 532 nm. n_{env} is the refractive index of the working enviroment of the MO. Computing all the numbers we get a $\mathrm{K}_{\mathsf{magnon,max}} \approx 17.7\,\mu\mathsf{m}^{-1}$ [38, 14]. BLS is only intensity sensitive, and not phase sensitive and thus only standing waves can be spatially resolved but propagating waves can not.

3.4 Frequency Resolved Magneto-Optic Kerr Effect

The setup for frequency resolved magneto-optic kerr effect (FRMOKE) is shown in Fig. 3.7. The linearly polarized light with wavelength $\lambda = 532.2\,\text{nm}$ is directed into a Glan-Thompson (GT) polarizer, where the light is split into an ordinary and extraordinary light paths, due to its inherently anisotropic crystalline structure [40]. GT polarizer is typically made of calcite, and therefore light suffers birefringence effect [14]. Light is focussed on the sample surface with a microscope objective (NA=0.75), resulting in a diffraction limited laser sport diameter given by

$$D = \frac{0.61\lambda}{NA} \sim 430\,\text{nm}. \tag{3.12}$$

An external, static, magnetic field $\mathbf{H}_0$ is applied in the sample plane by an electromagnet.

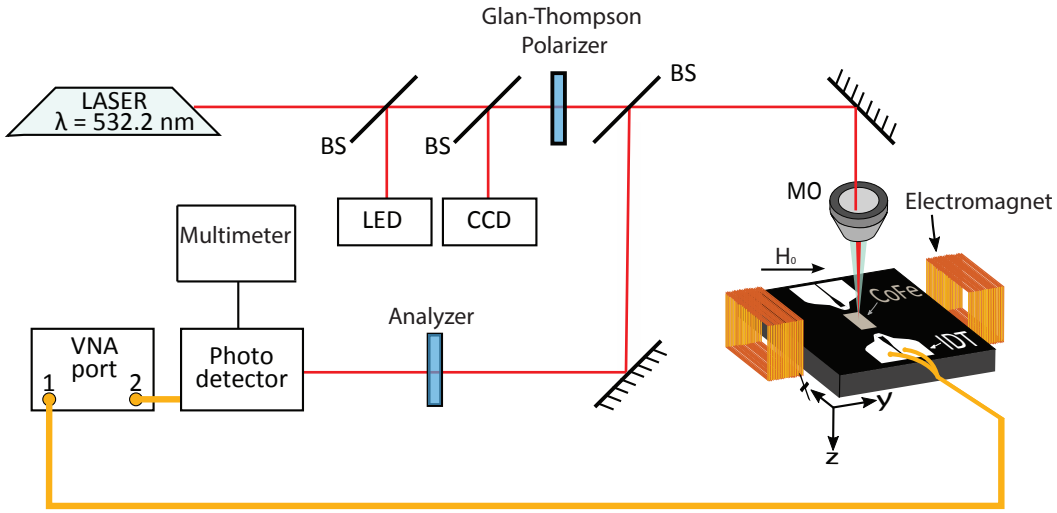

Figure 3.7: micro focused FRMOKE setup. Image adapted from [14].

The back-reflected light polarization is rotated due to the polar MOKE effect, stemming from the dynamic Out-Of-Plane (OOP) magnetization component m_z. The reflected light passes through a second polarizer, which is rotated 45° with respect to the GT polarization axis, The periodic change of the polarization angle is converted into a change of the laser intensity. Finally, this back-reflected light impinges on a photodector, where the signal is amplified and sent to port 2 of the VNA. The photodetector is also connected to a multimeter and therefore reflectivity measurements are possible.

With FRMOKE we are sensitive to both intensity and phase of the spin wave measurements, this is a critical difference to our BLS measurements. The port 1 of the VNA is connected to an IDT in our delay line thus applying a rf voltage, and therefore, generating a SAW.

4 Fabrication and Sample Preparation

The purpose of this section is to present the fabrication strategies used to fabricate all samples investigated in this thesis. Samples were patterned using Electron beam (Ebeam) lithography and optical lithography. Both patterning techniques are explained in the following and principal differences between them are discussed. The SUPERBOWL sputtering facility was used to metallize all of our samples and we thus introduce this magnetron sputtering tool and we comment some of the key aspects of magnetron sputtering deposition. As we have discussed in Sec. 2.2, LNO is the piezoelectric material used to excite SAWs as it is commonly used in SAW-based devices due to its high electromechanical coupling efficiency, which is around 5% [41, 9].

4.1 Micropatterning using Optical Lithography

The optical lithograpy tool used in this thesis, is the PicoMaster 200 laser writing module. The PicoMaster 200 laser writer consist mainly of a writing module and a sample holder. The writing module has a laser with wavelength of 405 nm. The sample fabrication during this thesis mostly follow the general scheme presented in Fig. 4.1.

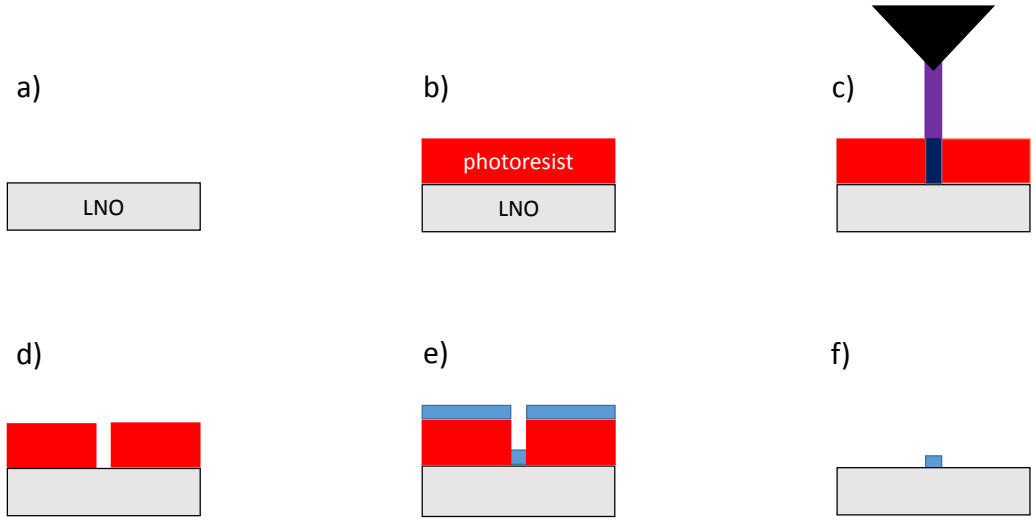

Figure 4.1: Scheme of all the involved steps in the fabrication process. a) LNO used as a clean substrate. b) photoresist is homogeously add on top of the clean substrate using a spin coatter. c) After the photoresist is added onto the substrate, the coatted substrated is irradiated with light, here light with wavelenngth of 405 nm. d) After light irradiaton, the irradiated sample is bathed in a developer which just removed the photoresist from the irradiated area. e) Metallization step using magnetron sputtering technique. d) after metallization, the sample is immersed in hot acetone and placed into a ultra sonic bath afterwards, this way the remaining photoresist is disolved. This figured is adapted from [38].

Typically we started with cleaning the substrate by immersing the LNO substrate inside a beaker with acetone. We placed the beaker in a ultra-sonic bath, set to the highest intensity. Inmediately after the ultra-sonic treatment we removed the acetone with IsoPropanol (IPA) by immersing the substrate into a beaker with IPA and placing it in the ultra-sonic bath at the highest intensity. After cleaning, the substrate was dryed with a nitrogen gun. Once the substrate was clean, we immediately placed it in the spin coater, in order to coat the substrate with a suitable photoresist spinning it . Immediately afterwards, we removed the surplus of photorist at the backside of the substrate using acetone. The photo-resist is soft-baked afterwards on a hotplate. This process minimizes dark erosion and increases adhesion to the substrate [42]. At this point, the substrate is ready to be used in the laser writer.

After exposure, we placed the exposed substrate in a developer, and thereafter into a beaker with clean water to stop the development process. A detailed list of all the parameters used for optical lithography can be found in Appendix. 9.2.

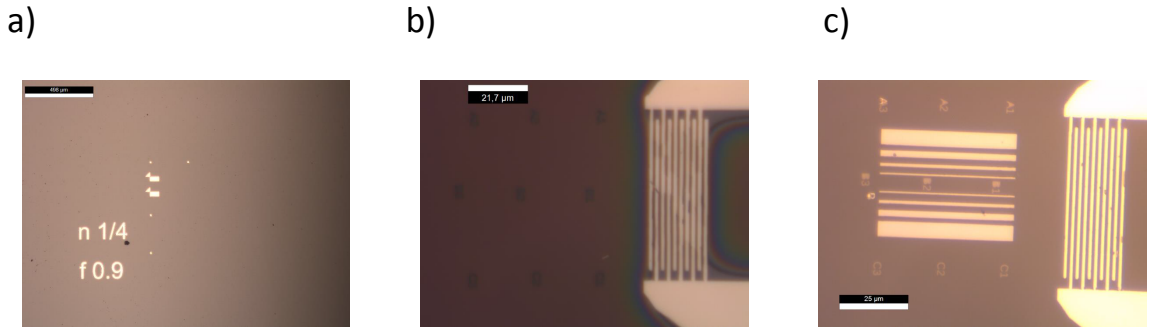

Figure 4.2: a) Micrograph of markers on a typical sample. These markers are used to get a perfect alignement between IDTs and CoFe. b) IDTs after metallization. c) CoFe strips after metallization

This fabrication process is divided in three different steps. In the first step we add the alignement markers, Fig. 4.2 a). In the second step the IDTs are added to the structure as shown in Fig. 4.2 b). we finally placed the ferromagnet, in this case the aforementioned CoFe between the IDTs as shown in Fig. 4.2 c).

4.2 Electron Beam Lithography

In addition to optical lithography, we also employed electron beam lithography to obtain smaller possible feature sizes for our IDTs. The e-beam process is similar to the optical lithography as shown in Fig. 4.3.

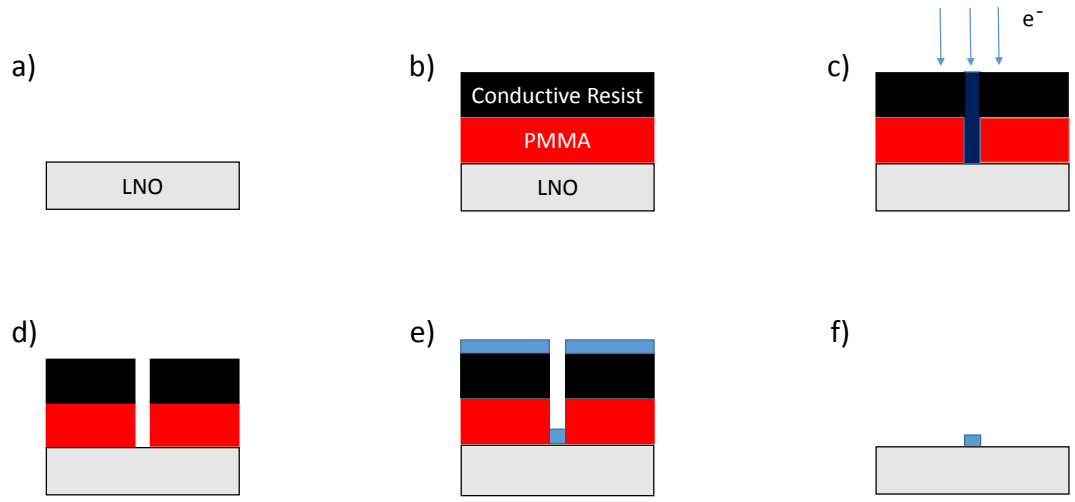

Figure 4.3: a) LNO used as a clean substrate. b) PMMA is homogeously add on top of the clean substrate using a spin coatter. In a second step, CR is added. c) After the PMMA and CR are added onto the substrate, the coatted substrated is irradiated with electrons. d) After electron irradiaton, the irradiated sample is bathed in a developer which just removed the PMMA and CR is removed with water from the irradiated area. e) Metallization step using magnetron sputtering technique. d) after metallization, the sample is immersed in hot acetone and placed into a ultra sonic bath afterwards, this way the remaining PMMA is disolved.

Black LNO is used as a clean substrate. A sensitive e-beam resist is homogeously added on top of the clean substrate using a spin coatter. Optical lithography limits the minimal feature size but is generally more reliable on electrically insulating substrates, because there are no charging effects. To avoid charging effects, here a Conductive Resist (CR) is used for e-beam exposure. After resist is added onto the substrate, the substrate is baked on a hot plate. After baking the sample, CR is added on the sample and soft-baked again on a hot plate. Once the sample is coated is ready to be irradiated with electrons in the e-beam. After electron irradiaton, the irradiated sample is immersed in clean water, which remove the CR. Thereafter, the sample is immersed in a developer, which remove the resist from the irradiated area. The developer is removed using clean IPA. Thereafter the sample is metallized using magnetron sputtering technique. After metallization, the sample is immersed in hot acetone

and placed in a ultra-sonic bath afterwards, this way the remaining photoresist is disolved in a lift-off process. A set of tables with all the parameters used for electron beam lithography is presented in Appendix. 9.1.

Just for comparison, a table with the time need for a sample fabrication with electron beam lithography and optical lithography is presented.

	electron beam (run time)	Optical lithography (estimated)
CoFe	1 min. 37 sec.	2 min.
IDTs	1 h. 41 m.	1h. 20 min.
Markers	4 m. 42 sec.	3 min.

Table 1: Times needed for fabrication for electron beam and optical lithography.

In addition to the times needed for lithography, which are very similar an extra time for pumping/venting the airlock in the e-beam is required, since the laser writer does not need any vacuum. This extra waiting time of approximately 1 hour for each step, makes the optical lithography with laser writer more favorable in terms of time needed to fabricate one working sample in comparison to e-beam lithography.

4.3 Magnetron Sputter Deposition

All measured samples were metallized using the SUPERBOWL Ultra High Vacuum (UHV) sputtering machine. The sputtering technique is based on basics of sputtering techniques is to accelerating positively charged particles, in this case Ar^+, as shown in Fig. 4.4 towards a high purity target material. Once the charged particle is directed to the target and therefore collide with the target a casacade of atoms from the target material, represented by M in Fig. 4.4, and secondary electrons are generated. Due to collision of atoms in the target material and secondary electrons, they will eventually leave the target.

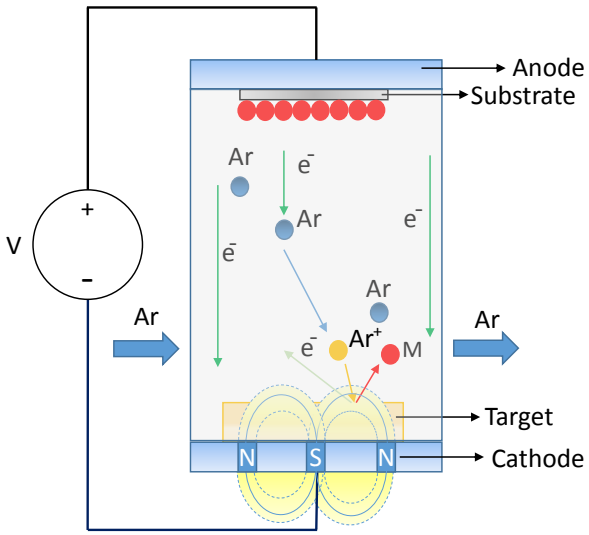

Figure 4.4: Magnetron sputtering technique is shown schematically. The usage of magnetic fields, increases the amount of plasma near the target, this way the deposition rate is increased.

We can take advantage of this, and place our substrate close enough to the target, and all particles emmited from the target can be adsorbed by the subtrate. This process takes place at very low deposition pressure. Such that the atoms coming from the target can travel without collision from the target to the sample. However a low pressure during to the depossition process leads to a lower amount of gas atoms that can be ionized and therefore less amount of charged particles can collide with the target and the probability of removing atoms from the target is lower [38], thus reducing the deposition rate. This issue can be solved by using a magnetron sputtering technique. This technique uses magnetic fields to confine the electrons close to the target where they can collide with the gas atoms as shown

in Fig.4.4, thus producing more plasma for increased deposition rate. A detailed list with all the parameters used for sputtering deposition can be found in Appendix. 9.3

5 Microwave Spectroscopy

In this chapter we present some of the key aspects of performing microwave spectroscopy on IDTs and SAW delay lines. We will discuss IDT performance and their characterization. The spectroscopy allows us to determine how much of the radio frequency (rf) voltage applied to the IDT is transformed into acoustic power. We also discuss the IDT insertion loss. Thereafter, a short disccusion about how to excite SAWs at higher harmonics of the fundamental frequency is introduced. The magnetic field dependence of the SAW transmission trhough a delay line loaded with a ferromagnetic thin film data will be presented. We show that with our IDTs we can drive FMR in our ferromagnetic (CoFe) thin films, showing the typical resonance-like features in our VNA transmission data as a function of the external applied magnetic field. Aditionally, measurements depending on the angle enclose by the SAW propagation direction and the direction of the applied external magnetic field are discussed. Finally, we compare our results obtained using CoFe with the results obtained in previous works, in which Ni was used as the ferromagnetic thin film.

5.1 IDT Characterization

To investigate phonon-magnon interaction, we need of certain devices that could provide certain conditions, that are required before hand. Ferromagnetic resonance frequencies are typically in the GHz frequency regime with the typical sound velocity LNO is $C_{\mathrm{LNO}} \sim 3500\,\mathrm{m/s}$ [43]; SAW wavelengths in the μm regime are thus needed. For excitation of such SAWs, IDTs with finger widths of typically bellow 1 μm. Such micropatterned IDTs are well stablished, as we have introduced in chapter. 4. Before studying the magnon-phonon interaction, we characterize the SAW transmission through delay lines formed by two opposing IDTs as schematically shown in Fig. 5.1.a).

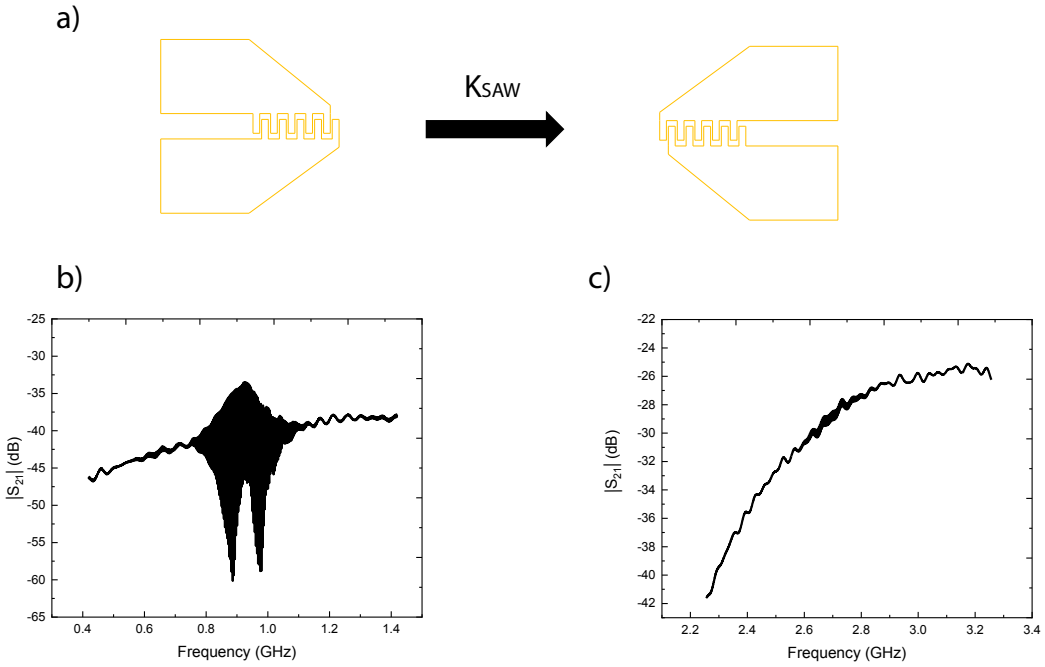

Figure 5.1: a) Typical SAW delay line, with finger overlap 50 µm, and a number of finger pairs of 5. The distance between IDTs is 1 mm corresponding to the SAW delay line used to obtain the data in b) and c). b) and c) typical spectra recorded for the transmission after a VNA measurement. The fundamental frequency is about 0.91 GHz, the frequency for the third harmonic is 2.73 GHz. To separate the SAW signal from spurious microwave crosstalk the data can be processed by a time gatting algorithm, as explained in Sec. 3.2.

To this end, we measure the transmission S_{21} through a typical SAW delay line. Data in Fig. 5.1.b) shows S_{21} around the fundamental IDT frequency of about 0.91 GHz, while data in Fig. 5.1.c) shows S_{21} around the third harmonic (2.73 GHz). As discussed in the previous section, to clearly distinguish between the EMW crosstalk and the SAW we apply the inverse Fourier transformation to raw S_{21}vs f data. The SAW and electromagnetic signals have different propagation velocities allowing to disentagle them in the time domain data shown in Fig. 5.2. The presence of the EMW signal is coming from the fact that we apply a rf voltage to the input IDT. The EMW is then radiated from the fingers of the input IDT and

travels along the delay line with the speed of light, and is detected at the second, output, IDT. As we know from the design, the distance between input and output IDTs is set to be $d_{IDT} = 1\,mm$. We thus expect the EMW signal to appear almost immediately in the time domain data. However, this signal appears with a delay of some nanoseconds due to the several meter long microwave cables. The sound velocity in LNO is about C_{LNO} ~3500 m/s, so we would expect the SAW signal to be at $t_{SAW} = d_{IDT}/C_{LNO} = 0.33$ µs in full agreement with data in Fig. 5.2. In previous works done at the Walther-Meissner-Institut (WMI) a triple transit signal was also found. The triple transit signal is just the time that the SAW needs to travel 3 times through the delay line. In our measurements, this signal was found but was too small to be significant in comparison with the EMW and SAW contributions. We attribute this negligible contribution to the triplet transit because the SAW was mostly attenuated by the CoFe thin film due to Insertion Loss (IL), which is a parameter used to characterize RF networks. IL is the signal loss power given by the insertion of a device in the SAW delay line. IL is given by [34]

$$\mathrm{IL} = \frac{P_{\mathrm{out}}}{P_{\mathrm{in}}} = \frac{|S_{21}|^2}{1 - |S_{11}|^2}, \tag{5.1}$$

only when the RF voltage is applied to one of the IDTs. Another possible reason for the SAW attenuation could be attributed to air loading [44].

From Fig. 5.2. we notice that for the first harmonic the SAW signal and the EMW signal are of comparable magnitude. However, for the third harmonic the SAW is smaller than the EMW. We attribute this to higher efficiency for SAW generation at the first harmonic frequency, compared to higher harmonics, due to 3 different mechanisms [44]: i) Interaction with thermally excited elastic waves. ii) Scattering by cristalline defects and surface scratches. iii) Energy lost due to air adjacent to the surface. This result is also well established as demonstrated in previous works [14, 9].

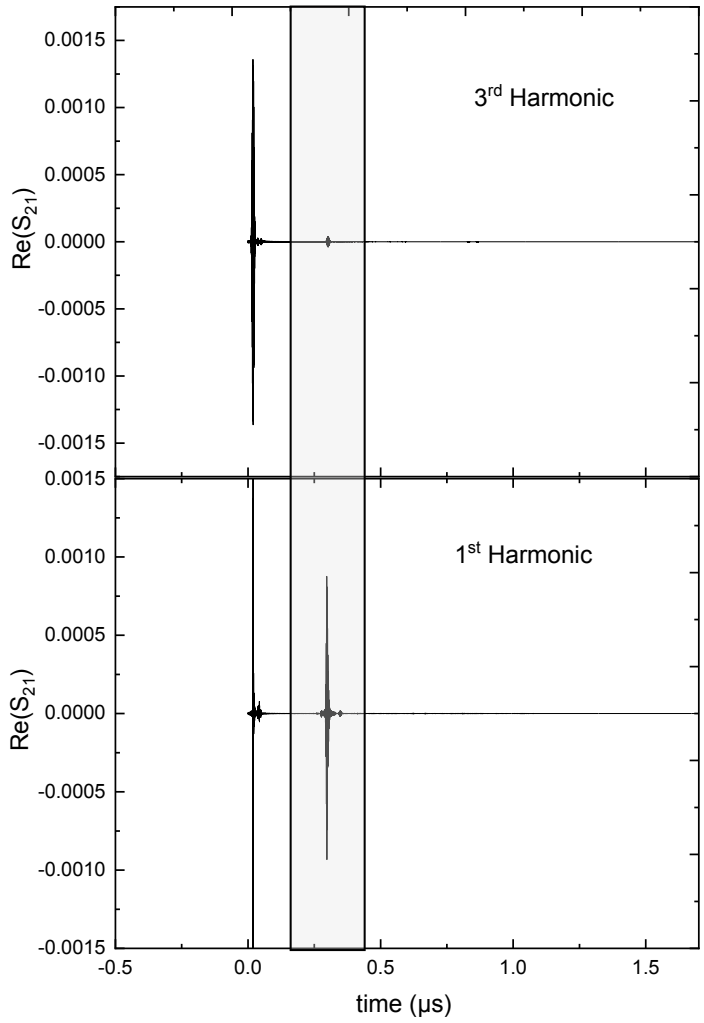

Figure 5.2: Real part of the S_{21} transmission parameter. Shown are the 1st and the 3rd harmonics. We can see the two main contributions to the signals. The first signal corresponds to the EMW and the second one (highlighted with grey background) corresponds to the SAW signal.

We now discuss the frequency response of the IDT, $X_{IDT}(f)$. From the evalution of this frequency response one can extract the magnitude, as schematically shown in Fig. 5.3.a) and b) represented with the red line. This function basically depends on the number of finger pairs of the IDT, the total number of electrodes and, the center frequency. The frequency evolution of $|X_{IDT}(f)|$ can be approximated by a sinc function [45]

$$|X_{IDT}(f)| \approx N_e \left| \frac{\sin(N\pi(f - f_0)/f_0)}{N\pi(f - f_0)/f_0} \right|. \tag{5.2}$$

Wehere N is the total number of finger pairs and N_e is the total number of electrodes. This response function can be easily understood as the sinc function is just the fourier transformation of the delta functions representing the rectangular potencial applied to every finger,

as schematically shown in Fig. (5.3).c). We assume each finger to be only a line charge. This is the so called delta-function model of the IDT [45], the surface potential is a succession of delta functions with alternating polarity. The total amplitude is given by the total number of electrodes. The SAW wavelength λ is given by the spacing between consecutive fingers (g) and the finger width w, as λ =2($g + w$). The frequency is then given by $f = \frac{C_{LNO}}{\lambda}$ as shown in Fig. 5.3.d) the expected response for the transmission function will be a sinc^2 if we investigate delay lines formed by 2 identical IDTs, as shown in Fig. 5.3.a) and b), which is the case we are studying within this thesis.

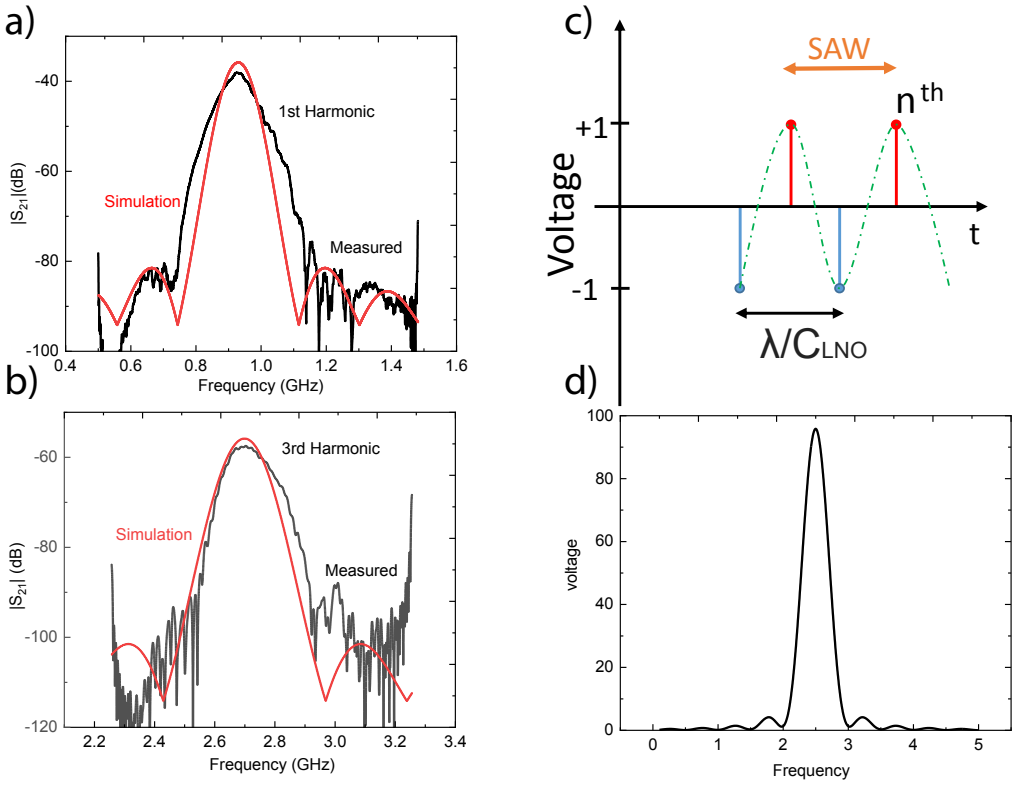

Figure 5.3: a) and b) measured transmission parameter as a function of the frequency in black, the red curve is the frequency response function given in Eq. 5.2. c) we model the fingers of the IDTs as a periodic potential, every finger is mathematically understood as a delta function. The SAW, then, propagates to the right and to the left. It is very important to take into account this bidirectionality of the IDT to calculate the acoustic power properly. This image is adapted from [9] d) Calculated transmission of a delay line as a function of the frequency. The general form is a sinc^2 function if we consider both IDTs to be identical.

Another important parameter involved in the study and characterization of IDT, is the so-called metallization ratio. The metallization ratio is defined as the ratio between the finger width and the space between two consecutive fingers

$$\eta = \frac{w}{g}. \tag{5.3}$$

In all our devices we kept the metallization ratio $\eta = 1$. The election of this number for the metalization ratio is not arbitrary, and the reason is based on the following consideration. In principle, every odd harmonic is susceptible of being excited by an IDT, however, the excitation efficiency depends on mode number and η. The derivation of the relation between the excited harmonic amplitudes and the metallization ratio can be found in [46]. The relation is given by

$$A_{2n+1} \propto \frac{P_n\left(2\cos^2\left(\frac{\pi}{2}(1-\eta)\right)-1\right)}{K\left(1-\cos\left(\frac{\pi}{2}(1-\eta)\right)\right)}, \tag{5.4}$$

where $A_{2n+1}$is the amplitude of the $(2n+1)^{th}$ harmonic, P_n is the n^{th} Legendre polynomial and K is the complete elliptic integral of the first kind. A_{2n+1} is shown in Fig. 5.4 as a function of η. We can observe that $\eta = 1$ allows to excite all odd harmonics with maximum amplitude.

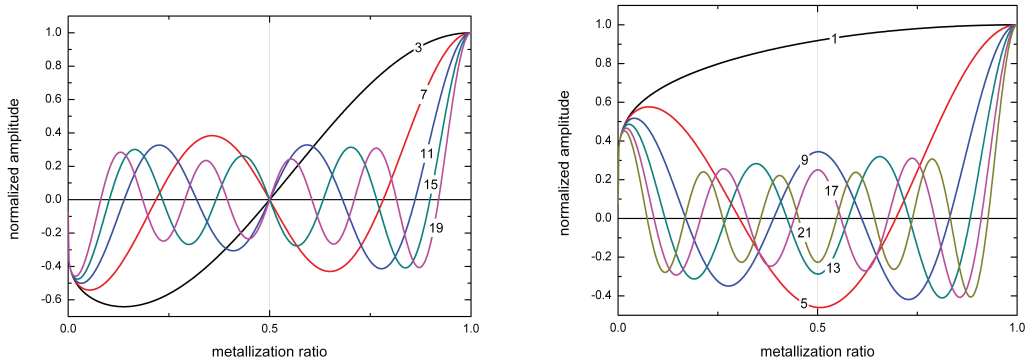

Figure 5.4: This image show the normalized amplitude of odd harmonics up to the 21^{th}harmonic as a function of the metalization ratio. This image is taken from [47]

We now consider the efficiency of an IDT to generate and detect SAWs. For this purpose a measurement of the reflection coefficient S_{11} is, indeed, neccessary. The dip in $|S_{11}|^2$ at f=0.91 GHz shown in Fig. 5.5.a) is due to the excitation of a SAW. From Fig.5.5.a) and b) we can extract the efficiency G to generate a SAW. We estimate the efficiency to generate a SAW to be roughly G=27% from Fig. 5.5

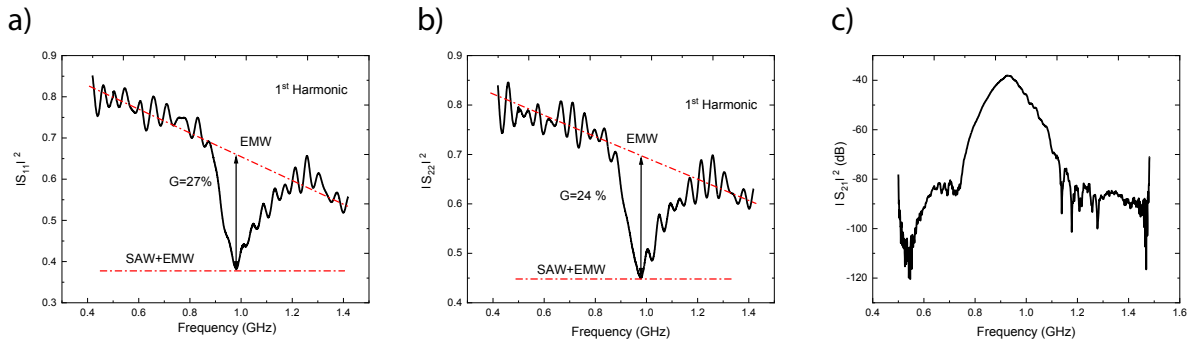

Figure 5.5: a) Measured $|S_{11}|^2$ as a function of the frequency for the first harmonic. G=$|S_{11}|^2$ (EMW) − $|S_{11}|^2$ (EMW + SAW) is a measure of the power conversion efficiency at port 1. b) Measured $|S_{22}|^2$as a function of the frequency at port 2, the power conversion efficiency is slightly different compared to port 1, indicating that both IDTs are not identical. c) $|S_{21}|^2$is a measure of how identical IDTs are.

From this value we can calculate the power of the SAW launched towards the CoFe thin film as

$$P_{\mathrm{SAW}} = \frac{1}{2} \mathrm{G} P_{\mathrm{rf}}, \tag{5.5}$$

the factor $\frac{1}{2}$ takes into account the bidirectionality of the IDT, thus the SAW generated by an IDT propagates one half to the right and one half to the left. P_{rf} is the radio frequency power applied to the input IDT, which in general is given in dBm. The dBm is a very common unit used in radio-frequency communication networks to express power ratio referred to 1 mW in dB. The relation is given by

$$\mathrm{dBm} = 10\log(\mathrm{P}/1\,\mathrm{mW}), \tag{5.6}$$

in all our measurements we applied 12 dBm to our input IDT, thus according to Eq. (5.6). approximately 16 mW. Thies yields $P_{\mathrm{SAW}} = 2.48\,\mathrm{mW}$ from Eq. (5.5). Finally, we can conclude how identical are the IDTs, by observing Fig. 5.5. According to Fig. 5.5.a) the SAW conversion efficiency is about 27%, thus according to expectations, we expect a value of $|S_{21}|^2 = \left(\frac{1}{2}\mathrm{G}\right)^2 = -23$ dB. From Fig. 5.5.c) we can extract a value of $|S_{21}|^2 = -37$ dB, these two different values indicate that we have either non identical IDTs, something expected, according to Fig. 5.5.a) and b) or SAW propagation loss.

5.2 Delay Line Transmission Measurements with Magnetic Field

In this section, we investigate the influence of an applied external magnetic field on our S_{21} transmission data. The magnitude of the applied external magnetic field and also the angle that the external magnetic field encloses with the propagation direction of the SAW affects the tranmission signal, as exemplarily shown in Fig. 5.6. Furthermore, we compare the results obtained in CoFe to those obtained in previous works with Nickel (Ni).

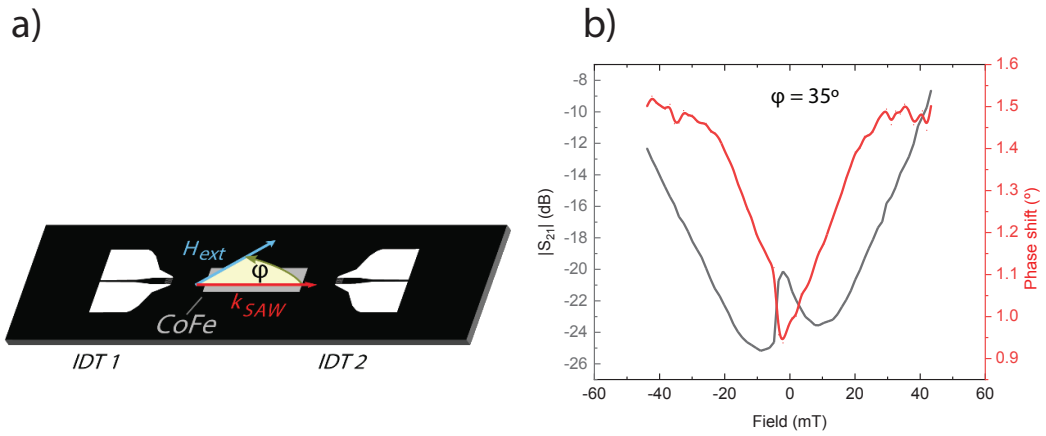

Figure 5.6: a) Angle enclosed by SAW propagation direction and externally applied magnetic field. b) After timegating algorithm is applied to the VNA data, a clear resonance peak and a phase shift are visible.

The coupling between the magnetization **M** and the SAW results in a resonant attenuation and phase shift of the SAW transmission when the condition for FMR is met, as exemplarily shown in Fig. 5.6. With structured SAW delay lines loaded with a ferromagnetic thin film we can study the interaction between magnons and phonons in the GHz regime. For illustrative purposes we have used "AG_SAW_001" sample, with a 20 nm CoFe thin film between both IDTs as shown in Fig. 5.6.a). For a detailed description of all parameters e.g. lateral dimensions, number of finger pairs, CoFe thickness, etc... refer to Apendix.9.4. An homogeneous, in plane $\mu_0 H_{ext}$, is applied to the system. The magnitude of the applied magnetic field and also its direction with respect the SAW propagation direction affects the transmission signal. We use time-gated data, so we can exclude that the magnetic field dependence is produced by the EMW. Thus, the magnetic field dependent data can only be caused by changes in the SAW amplitude and phase.

The data shown in Fig. 5.7 corresponds to the third harmonic, in particular a magnetic field down-sweep was performed. Two main features can be extracted from the measurement. First, very close to zero applied external magnetic field, a hysteretic, sharp, dip is visible. For 0° and 8° only this hysteretic behaviour is visible. The sharp peak is also visible for

larger angles, e.g., $\varphi = 35°, 45°, 60°$. The switching of the ferromagnet causes a change in the elastic properties of the CoFe thin film due to magnetostriction [30]. The switching of the ferromagnet, closely corresponds to the value for the coercive field, $\mu_0 H_{ext} \sim 2\,mT$, in CoFe [48]. Second, two non-hysteretic dips in $|S_{21}|$ are clearly visible for $\varphi = 35°, 45°, 60°$. However, they appear at different values of $\mu_0 H_{ext}$ due to the in-plane magnetic anisotropy in the CoFe thin film. This result is well established as demonstrated in previous works done at the Walther-Meissner-Institut (WMI) [9, 34, 14]. These dips are attributed to a resonant interaction of the SAW and spin-waves in the CoFe thin film.

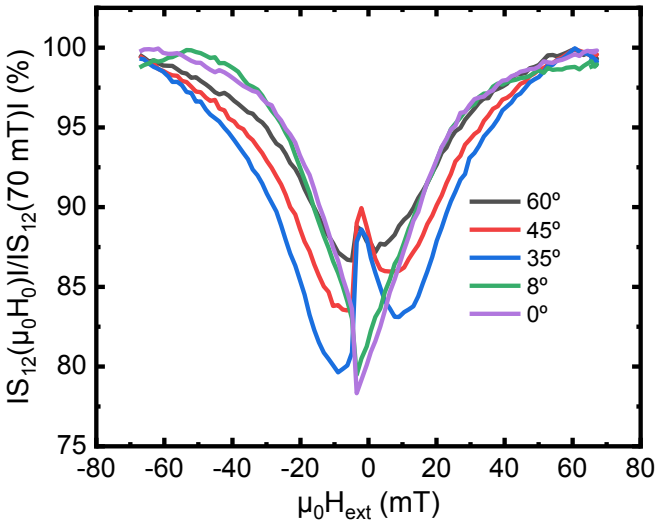

Figure 5.7: Time-gated data for the $|S_{21}|$ transmission as a function of the external magnetic field normalized to the data obtained at 70 mT.

From Fig. 5.7 we find that the minimum $|S_{21}|$ is found at larges $|\mu_0 H_{ext}|$ for an angle of $\varphi = 35°$, leading to clearly separated resonance dips for this orientation. For this reason, we kept this orientation for the rest of the measurements within this thesis.

Now, we want to give an explanation of why we see this angle dependent behaviour shown in Fig. 5.7. A description based in the LLG equation Eq. (2.2) including elastic strains is used to explain why we see the resonant peaks only for certain angles of H_{ext} with respect the SAW propagation direction. The Stoner-Wohlfarth approach [49] and therefore, domain formation and magnetic switching are not taken into account. Typically, in normal FM thin films the free energy is determined by the externally applied magnetic field and the magnetic anisotropy, in particular, for an in-plane applied magnetic field, which is the case studied here. The free energy of the thin film in the static limit is given by [9]

$$F_{DC} = -\mu_0 \mathbf{H} \cdot \mathbf{m} + B_d m_z^2 + B_u (u \cdot m)^2 , \tag{5.7}$$

where the first term on the right side is the zeemann term and the second one is the

shape anisotropy, which basically keeps the magnetization in the film plane. The last term a uniaxial in-plane anisotropy [34]. The free energy contribution due to magnetoelastic interaction with the SAW is given by Eq. (2.7), in total we have a total free energy contribution $F = F_{DC} + F_{AC}$. The effective magnetic field, used in Eq. (2.2) is given by

$$\mu_0 H_{eff} = -\nabla_{\mathbf{m}} F = -\nabla_{\mathbf{m}}(F_{AC} + F_{DC}). \tag{5.8}$$

According to the reference frame introduced in Fig. 2.5, it is clear that the condition for ADFMR is dependent on the angles formed by the magnetization and the externally applied magnetic field within the film plane. The magnetic anisotropy F_{DC} is responsible for the peaks position on $\mu_0 H_{ext}$, as shown in Fig. 5.8.a), while the magnetoelasticity is responsible for the dip amplitude, as exemplarily shown in Fig. 5.8.b) where the magnetoeslastic driving field is shown as a fuction of ϕ_0 and $\theta_0 = 90^o$ for the IP-configuration, in the ideal case.

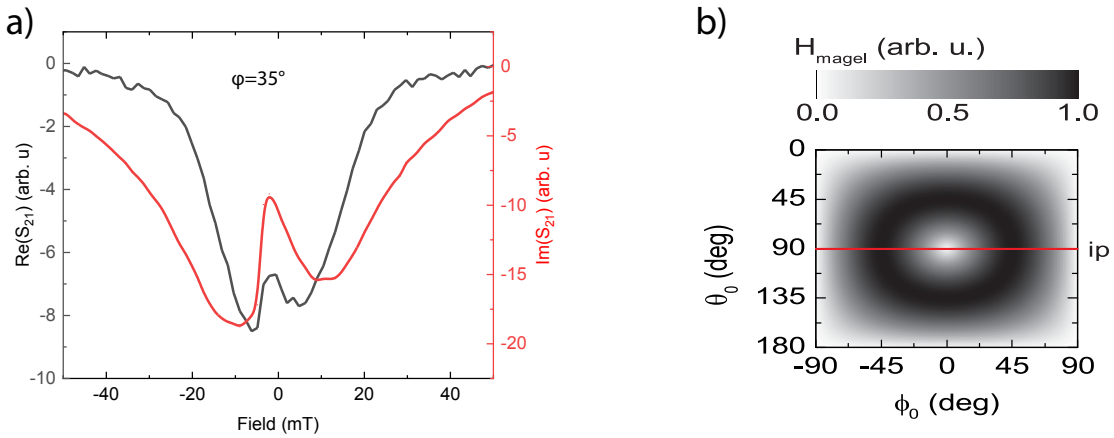

Figure 5.8: a) real and imaginary part of the $|S_{21}|$ as a function of the externally applied magnetic field. b) Dip position as a function of ϕ_0 and θ_0= 90^o, the case studied within this thesis. This image is adapted from [9].

Now we investigate if the magnetic field at which we see the magnetic resonance is comparable to theoretical values. In conventional FMR studies some magnetic properties e.g., the magnetization saturation and the gyromagnetic ratio are studied rotating the sample in the plane of the film. The relation between these parameters is given by the In-plane Kittel equation [38]

$$\mu_0 H_{res,t} = \sqrt{\frac{f^2}{(g\mu_B/h)^2} + \frac{(\mu_0 M_{eff})^2}{4}} - \mu_0 H_{aniso,IP} - \frac{\mu_0 M_{eff}}{2}, \tag{5.9}$$

where $H_{res,t}$ is the value at which we expect the resonance, g is the Landè-factor and M_{eff} is the effective magnetization saturation, given by

$$M_{eff} = H_{aniso} + M_{saturation}, \tag{5.10}$$

where H_{aniso} is the anisotropy contribution and $M_{saturation}$. Eq. (5.9) yields $\mu_0 H_{res,t} \sim 4\,mT$ ($g = 2.06624$ and $\mu_0 M_{eff} = 2.406\,T$ [38]). From Fig. 5.7.b) we observe a value $\mu_0 H_{res} \sim 8.0\,mT$.

Finally, we study the SAW attenuation and we compare it with previous works done with Ni thin films. C. Heeg [34] described the maximun SAW attenuation by

$$\Lambda = |\text{Min. } |S_{21}(f, H)|| \tag{5.11}$$

Of course, Λ is also dependent on the external magnetic field orientation and frequency. In previous works C. Heeg [34] found a value of $\Lambda = 500\,dB/cm$ for a Ni thin film of 50 nm thickness at a frequency of f=2.93 GHz and an angle of $\varphi = 30^o$. Similar results where found also in a 25 nm thick Ni thin film, for a frequency of f = 1.99 GHz and $\varphi = 40^o$, [50] with a reported value of 312 dB/cm. We report a value of 369 dB/cm for our 20 nm thick CoFe thin film at f=2.73 GHz and $\varphi = 35^o$.

6 Optical spectroscopy

In this chapter, spatially resolved SAW data and spatially resolved SAW-magnon interactions data is presented. BLS setup and FRMOKE setup were both used to optically measure SAWs and SAW-spin wave interaction. On the one hand, BLS is sensitive to the spin-wave intensity, it is insensitive to the wavefronts of propagating waves, but it allows to spatially resolve standing waves, as we will see in the following sections. On the other hand, with FRMOKE we are able to optically detect travelling SAWs. The SAW-magnon interaction can be measured with both techniques, as we will show. Finally, results obtained with FRMOKE and BLS are compared with results obtained with microwave spectroscopy.

6.1 Spatially resolved surface acoustic waves

In this section we present results about optically detected SAWs using the FROMKE [8] and BLS technique as a function of the laser spot position and externally applied magnetic field sterngth and orientation. In Fig. 6.1.a) a microscope image obtained during the FRMOKE measurement is shown. The red box indicates the area in which the laser spot was scanned. In Fig. 6.1.b) a photodetector measurement, showing the reflectivity along the highlighted area is shown. The reflectivity on CoFe is higher than the reflectivity on LNO. The SAW is propagating along the CoFe stripe, with 2 μm width and 45 μm length. For this particular measurement, an IDT with N = 5 finger pairs and a periodicity of p = 4 μm is used to launch the SAW, as shown in Fig. 6.2.a). Represented in red and blue are the maxima and minima of the real part of the S_{21} transmission parameter, respectively.

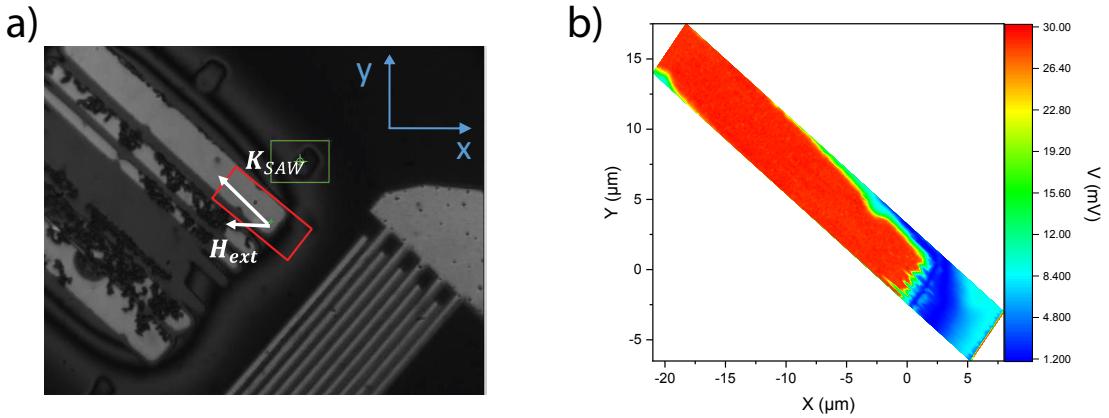

Figure 6.1: a) IDT and CoFe stripe used for a FRMOKE measurement. The propagation direction of the SAW and the direction of the externally applied magnetic field are shown. b) photodetector measurement used as a measure of the reflectivity within the area indicated by the red rectangle in a).

As exemplarily shown in Fig. 6.2.a) a SAW with a frequency of 0.93 GHz is generated by an IDT with a finger periodicity of 4 μm, thus resulting in a SAW with 4 μm wavelength. Parallel SAW wavefronts are observed. In Fig. 6.2.b) the third harmonic with a frequency of f = 2.73 GHz is shown, the corresponding SAW wavelength is λ= 1.33 μm. The wavefronts, in this case, are homogeneous outside the CoFe, however, once the SAW travels inside the CoFe stripe, the appearance of intereferences becomes evident.

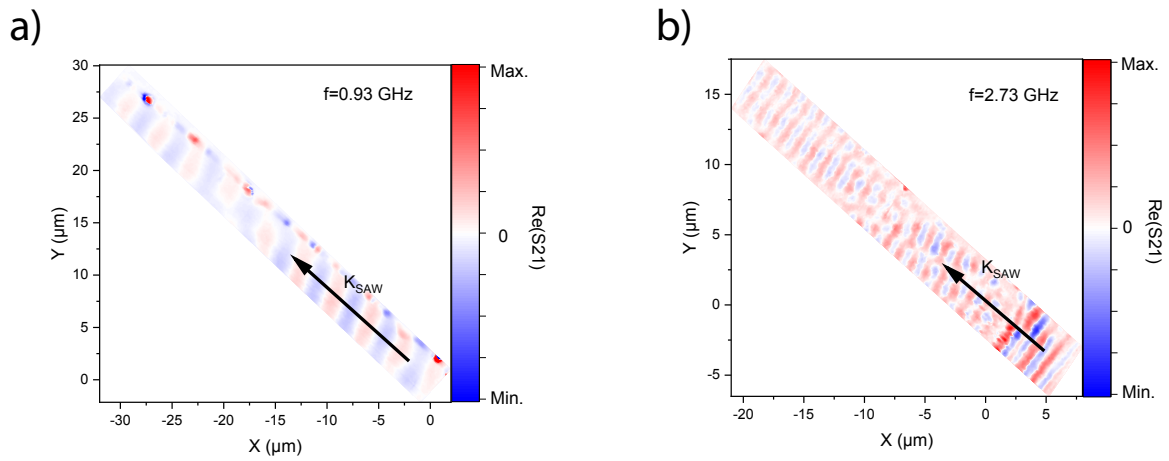

Figure 6.2: a) FRMOKE image of a SAW propagating with a frequency of 2.73 GHz. The wavefronts are clearly visible. b) FRMOKE image of a propagating SAW with 0.93 GHz, with parallel wavefronts.

The apperance of this intereference seem to increase with increasing frequency, as exemplarily shown for the 5$^{\text{th}}$ harmonic (f=4.55 GHz, $\lambda = 0.8$µm) in Fig. 6.3 where the interefence produces a very complicated wavefronts pattern. This interference probably stems from the fact that we have two different acoustic waves with different propagation velocities, one propagating trough the CoFe thin film and the other one propagating trough the LNO. At the edge of the CoFe stripe with the LNO, even for the first harmonic, the presence of the interference is visible. At even higher frequencies, the lateral resolution of the FRMOKE set up (approx. 500 nm) is insufficient to clearly image the SAW.

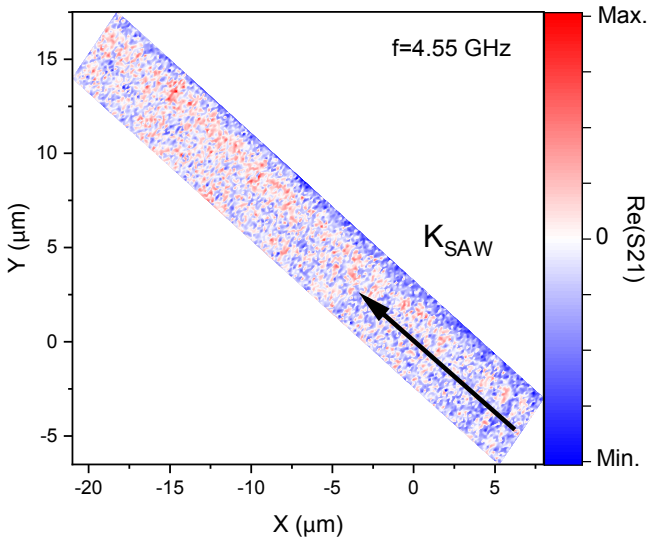

Figure 6.3: Real part of the S_{21} parameter as a function of the position for the 5$^{\text{th}}$ harmonic.

As we have already discussed in section 3.3, BLS spectroscopy is not phase sensitive, so we can not resolve wavefronts of travelling SAWs with this technique. However, standing

waves can be resolved, up to the limit given by the spatial resolution, given by Eq. (3.12). The apperance of an standing waves in this type of measurements was already reported by C. Mühlenhoff [14] in his Co thin films. In Fig. 6.4.a) the configuration used for a BLS measurements is shown. A rf voltage of 14 dBm was applied to the IDT, the angle enclosed by the propagation direction of the SAW and the externally applied magnetic field is set at $\varphi = 35^{\text{o}}$. A linescan going from outside to the CoFe thin film to inside was performed. A beating pattern with a wavelength of $\lambda \sim 22\,\mu$m was observed. The sharp influence of the standing wave, strongly suggested the presence of at least two different k-vectors.

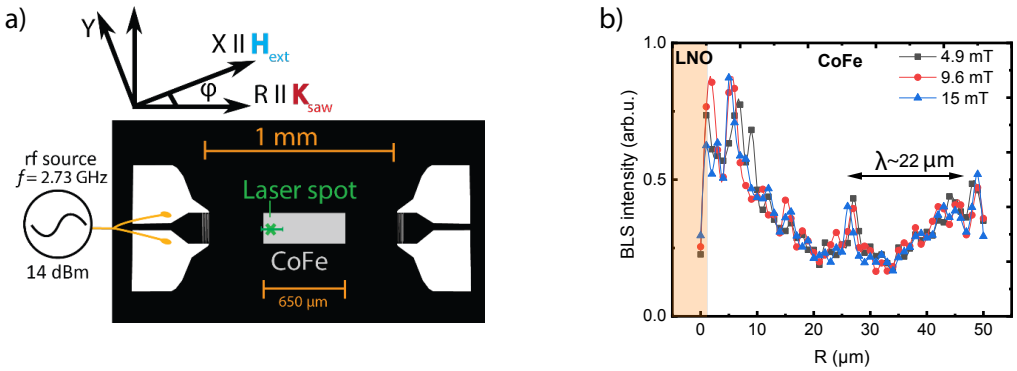

Figure 6.4: a) Laser spot position and linescan performed during a typical BLS measurement. b) linescans obtained for differents externally applied magnetic fields. A beating pattern with a wavelength of approximately 22 μm was found.

Another reason could be simultaneous detection of a SAW k-vector and a spin wave k-vector, differing from the SAW k-vector due to non-linear magnon dispersion relation. The dispersion relation for dipolar-exchange spin waves is [51]

$$\left(\frac{\omega}{\mu_0\gamma}\right)^2 = \left(\mathrm{H} + \mathrm{Jk}^2 + \mathrm{M} - \frac{\mathrm{Mkd}}{2}\right)\mathrm{x}\left(\mathrm{H} + \mathrm{Jk}^2 + \frac{\mathrm{Mkd}}{2}\sin^2\varphi\right), \tag{6.1}$$

Where d is the film thickness, M the saturation magnetization and J= $\left(\frac{2\mathrm{A}}{\mu_0\mathrm{M}}\right)$ with the exchange stiffness constant A. For the SAW phonons, the dispersion relation for small k-vectors is $\omega_{\text{phonon}} \propto$ k. Thus, a simultaneous matching of frequency, wavevector and group velocity is generally not possible between spin waves and SAWs. We speculate that this is the cause for the beating pattern observed in Fig. 5.4 b).

6.2 Spatially resolved SAW-Spinwave interaction

In this section, ADFMR measurements are presented and discussed. To optically detect magnon-phonon interaction, experimental techniques introduced in section 3.3 and section 3.4 were used. With our measurements, magnon-phonon coupling can be determined as a function of the external magnetic field, laser spot position and frequency.

In the first measurement done using the BLS setup we obtained a heat map in which the laser spot was scanned from outside the CoFe thin film to inside the thin film, as schematically shown in Fig. 6.4.a). Such linescans were performed for several values of the external magnetic field. The first feature, is that a vertical pattern for the magnetic response is found on the CoFe patch with a continous shift of $\Delta R = 4\,\mu m$. As we can see from Fig. 6.5, the observed pattern seems to be independent of the magnitude of the external magnetic field. This result is in contrast to the findings of C. Mühlenhoff in his master thesis [14] using Co, who observed a continous shift in the maximum BLS intensity with increasing the SAW path.

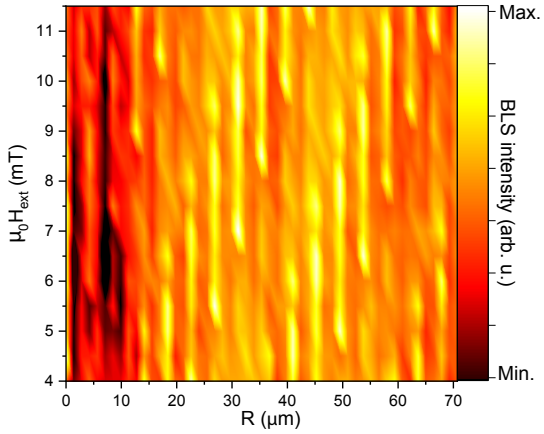

Figure 6.5: Heat-map with distance from outside the CoFe patch to inside of it as a function of the applied magnetic field. A parallel pattern is observed with a continous shift as a function of the SAW path.

Now, we try to understand this behaviour. To this end, we placed the laser spot at different distances inside the CoFe thin film, and we recorded a typical BLS spectrum. The frequency of the SAW was set to be around 2.73 GHz. From Fig. 6.6.a), b) and c) it is clear that the maximun BLS signal intensity, thus magnon creation (Stokes-peak), as shown with the black curve, is obtained for different magnitude of H_{ext} at different positions. This result was also observed by C. Mühlenhoff [14] in his Co thin films.Our results indicate a very complicated spacial interaction between magnons and phonons.

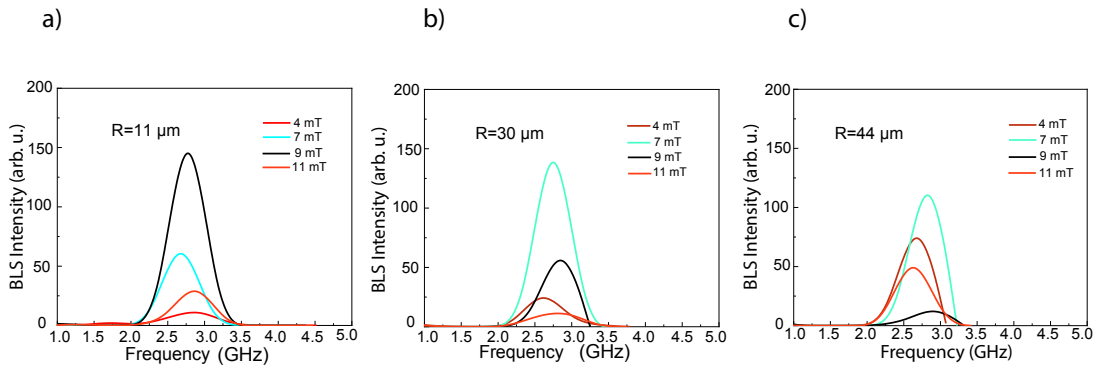

Figure 6.6: Stokes peak obtained with BLS setup at different position for different external magnetic fields.

We next performed a x-y BLS scan with a external magnetic field chosen to fullfill the conditions for ADFMR. Fig. 6.7.a) shows the measurement configuration with respect to the external magnetic field and the scanned area. As the highest amount of magnon generation is taking place at the CoFe beginning, as exemplarily show in Fig. 6.5 we have focused on this particular area. The externally applied magnetic field is set to be $\mu_0 H_{ext} = 9.2\,mT$. We set this particular value for the external magnetic field, as we expect conditions for ADFMR close to this value, as discussed in chapter 5.

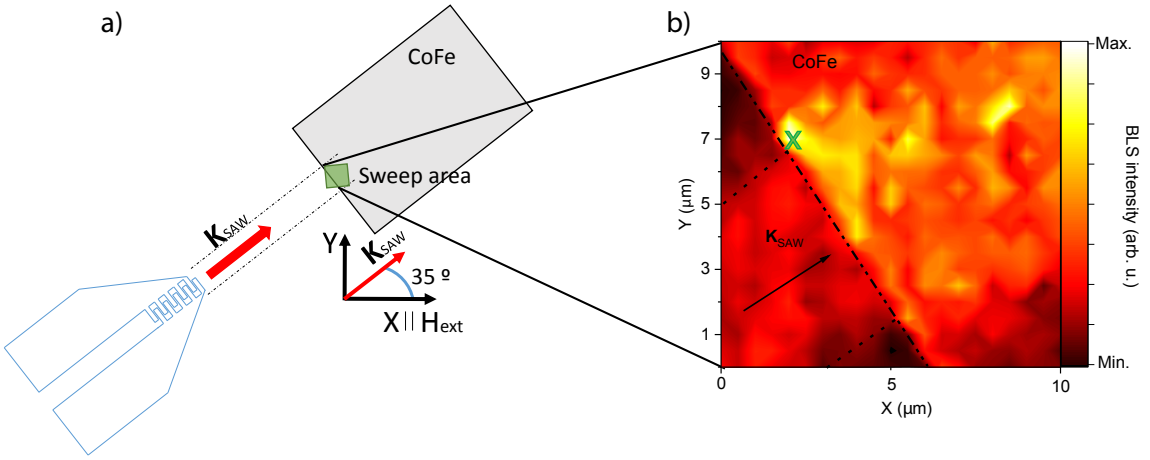

Figure 6.7: a) Schematic depiction of the geometry used for the 2-D scan at the CoFe beginning. The angle enclosed between the SAW k-vector and the external magnetic field is $\varphi = 35^{o}$. b) BLS intensity at f=2.73 GHz in the sweep area for $\mu_0 H_{ext} = 9.2$ mT, the green cross shows the laser spot position from the measurement taken in Fig. 6.8.

In Fig. 6.7.b) we plot the BLS intensity obtained within the area highlighted in green. We can see the path followed by the SAW and a huge amount of hot spots close to the CoFe edge, as we have expected from the results obtained in Fig. 6.5. In adittion to the huge amount of magnon generation at the CoFe edge, a very complicated pattern appears randomly distributed over the CoFe area. This strong spatial dependence of the magnon-

phonon interaction can be attributed to the formation of standing waves in the CoFe thin film due to the pressence of at least, two different k-vectors, as already disscussed in section 6.1. Now, we are interested in the magnetic response of the CoFe when placing the laser spot at a fixed position. Since the highest magnon generation is expected at the CoFe edge, we place the laser spot close to the edge as indicated by the cross in Fig. 6.7.b)

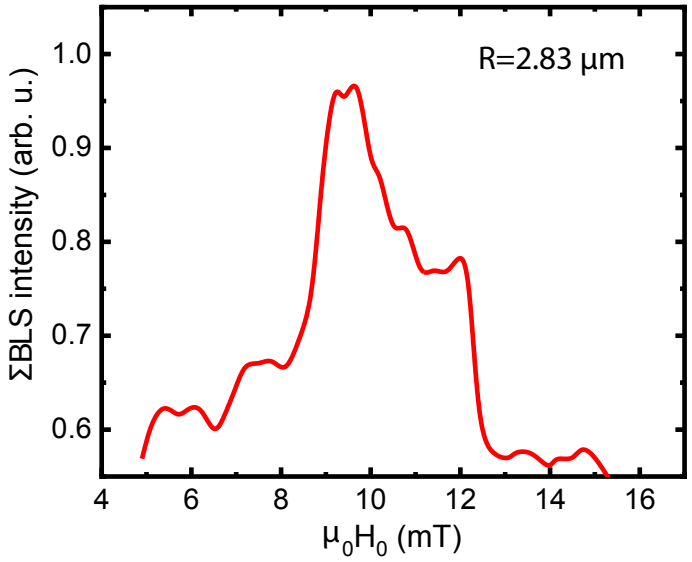

Figure 6.8: Normalized BLS intensity as a function of the external magnetic field. The laser spot is placed at R = 2.83 μm.

From Fig. 6.8 we can extract the maximum response of the BLS intensity at $\mu_0 H_{ext} \sim 9.5\,mT$. The laser spot was placed 1.83 μm awax from the CoFe edge, within the CoFe thin film. At this position, where the magnon generation has maximum efficiency, the extracted value of the resonance magnetic field matches very well with the observed value of the ADFMR feature observed with microwave spectroscopy in Fig. 5.7 for $\varphi = 35°$. We compare the results obtained with BLS spectroscopy to the VNA. Fig. 6.9 shows the magnetic response of the CoFe at the beginning of the CoFe patch obtained with BLS spectroscopy (red), together with the SAW transmission magnitude obtained with a VNA measurement (blue).

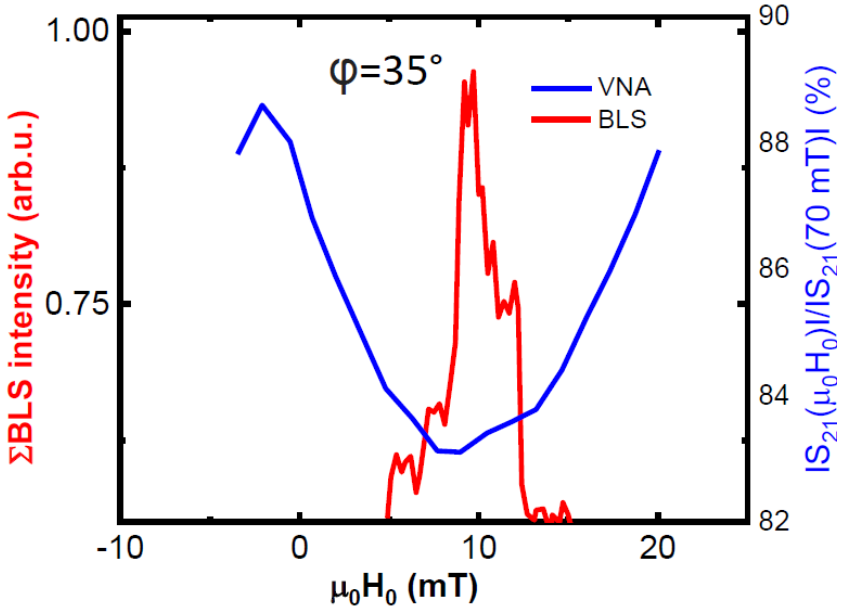

Figure 6.9: Normalized BLS intensity as a function of the external magnetic field vs. SAW transmission magnitude as a function of the external magnetic field. This result is in particular obtained for a frequency of 2.73 GHz.

The first observation is that both, the peak in the BLS intensity and the dip in the SAW transmission magnitude, show its relative extreme at around $\mu_0 H_{ext} \sim 10$ mT. This indicates that the FMR at this position on our CoFe (R=2.83 µm) thin film is indeed, acoustically driven. The second observation is a pronounced difference in linewidth for these two measurements on one and the same sample, which can be understood with the following argument. The measurement done to obtained the normalized BLS data was performed by placing the laser spot at a fix position and, therefore, only represents a local magnon-phonon interaction.In contrast, the VNA measurement takes into account the integral absorption of the SAW while traveling throughthe entire patch of CoFe. These results strongly indicate that the linewidth observed in the VNA-SAW measurements is inhomogeneously broadened due to interference between SAW and spinwaves. In the BLS measurements, narrow resonance linewidthts (as expected for CoFe) are recovered.

We performed FRMOKE measurements on the sample shown in Fig 6.1.a) as a function of external magnetic field.

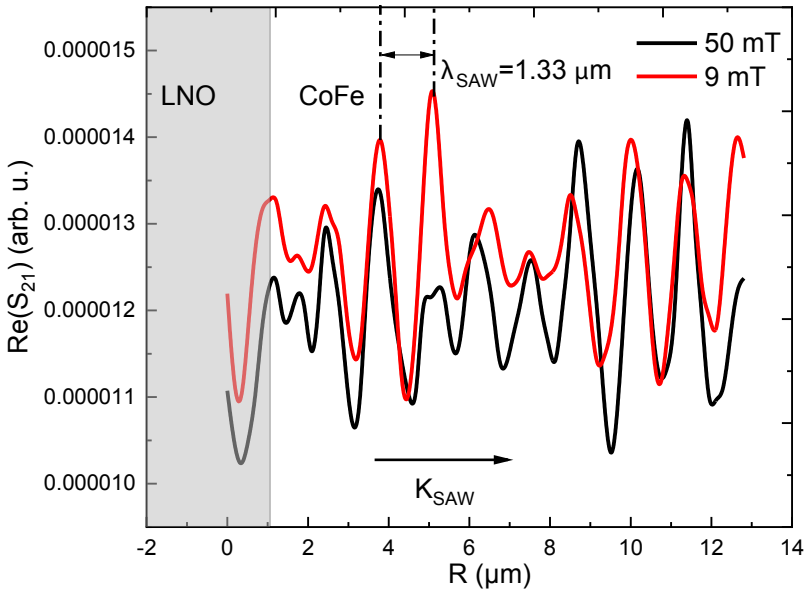

Figure 6.10: S_{21} expressed in dB as a function of the SAW path outside the CoFe and inside the CoFe. The arrow indicates the propagation direction of the SAW.

In Fig. 6.10, the real part of S_{21} as a function of the SAW path through the CoFe stripe is shown. In this particular sample, the travelling SAW wave can be observe with a wavelength of $\lambda_{SAW} = C_{LNO}/\nu \sim 1.33\,\mu$m as we would expect from the IDT design for the third harmonic (f=2.73 GHz). The black line is the data taken for $\mu_0 H_{ext} = 50$ mT, this is far away to the expected ADFMR condition. The red line taken at $\mu_0 H_{ext} = 9$ mT shows data inside the expected ADFMR conditions. We can observe that the maximum signal is obtained inside the CoFe stripe, a similar result is observed for BLS spectroscopy. This result is reproducible for several measurements.

Aditionally, we observed an increase of the SAW magnitude for the data obtained at 9 mT with respect the data obtained at 50 mT at peaks positions of the propagating wave. This result was also observed by C. Mühlenhoff [14] on Co thin films.

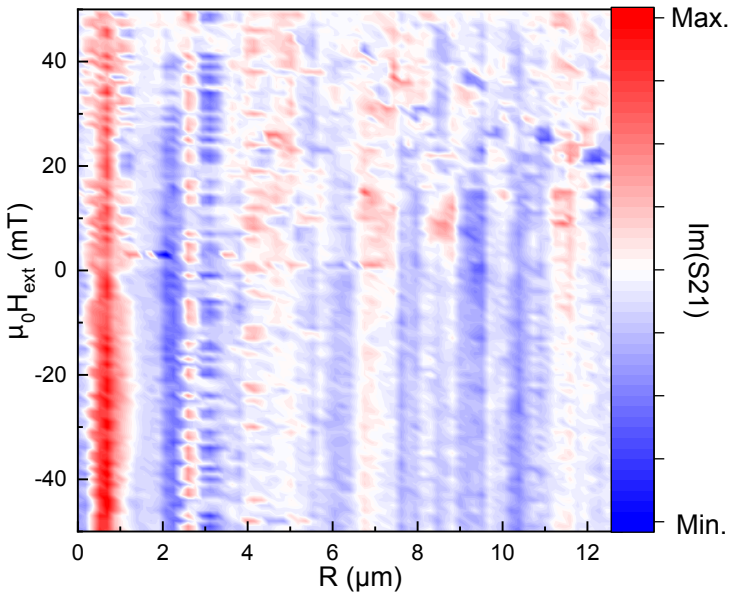

Figure 6.11: Heat map obtained for a FRMOKE measurement. Shown in the SAW path through the CoFe stripe as a function of the external magnetic field and the imaginary part of S_{21} transmission parameter, taking advantange of the phase resolved setup.

Finally, a heat map is shown in Fig. 6.11. we can see a vertical pattern indicating the position of the propagating magneto-acoustic wave peaks. However, we can observe a higher signal around $\mu_0 H_{ext} \sim 10\,mT$,at peak positions, inside the expected ADFMR as we have disscused in previous sections. Thus, we see a very similar magnon-phonon interaction mechanism on CoFe, than observed and reported on Co. Similar physics is, therfore, taking place in these two ferromagnetic materials.

7 Summary

Within this work, ADFMR measurements were performed using structured SAW delay lines loaded with a CoFe thin film to study the interaction between phonons and magnons. Samples were manufactured by optical lithography and e-beam on $LiNbO_3$ substrates. We performed microwave and optical spectroscopy on these samples and evaluated the results. In this chapter, we summarize the most important results and observations.

A VNA was used to characterize SAW delay lines. We used a time-gating algorithm to separate the direct electromagnetic crosstalk from the SAW contribution to the transmission S_{21}. Once the spectrum was cleaned from EMW, the study of SAW signal was reliable. As a first observation, we see that the signal strength is smaller for increasing frequency. This result is very well established as shown in previous works [9, 14, 34, 47]. Aditionally, the theoretically expected form of the SAW can be reproduced very well once the EMW contribution is neglected. By chosing an appropriate metallization ratio and higher harmonic frequency operation, we demonstrated operation of our IDT delay lines for frequencies up to 10 GHz. Furthermore, the conversion efficiency, G of the IDT from the applied rf voltage into strain is shown. the relation between the efficiency conversion and the SAW power is discussed and a value of $P_{SAW} = 2.48$ mW was found for our IDTs.

After the study and characterization of SAW delay lines the influence of both strength and the direction of an exteranlly applied magnetic field, $\mathbf{H}_{\mathsf{ext}}$ on S_{21} magnitude was studied. The presence of resonance-like at characteristic frequencies in our measurements combined with the zero contribution of the EMW due to signal processing, thus only leaving the contribution of the SAW to the signal, strongly suggest that the FMR is indeed acoustically driven. The presence of the resonance-like peaks in the S_{21} transmission data for different angles of the externally applied magnetic field, suggest that the coupling between phonons and magnons is stronger for certain directions of the SAW propagation with respect $\mathbf{H}_{\mathsf{ext}}$, in particular a value of $\varphi = 35°$ was found to be the best configuration to ensure the highest coupling between phonons and magnons in our CoFe thin films. We recovered the expected symmetry of SAW-driven FMR which has previously been studied in thin films of Ni and Co [14, 34, 9]. We compared the theoretical values of the magnetic field at which we would expect the resonance stemming from the phonon-magnon interaction. The observed and the measured values are very close and the difference between them arise from the in-plane anisotropy, which appears to be crucial for the magnetic properties of the FM thin films as shown in [38]. Furthermore the maximun SAW attenuation is discussed and compared to different material, yielding very similar values for SAWs propagating in CoFe and Ni thin films. CoFe thereby provides the advantage of much lower magnetic damping and higher saturation magnetization than Ni. This establishes CoFe as a promising material for magneto-acoustic devices.

We furthermore optically detected travelling SAWs through the CoFe thin film and spinwaves-SAW interaction using two different scanning-laser techniques. We found strong interference effects between SAW and spinwaves in our samples, demonstrating the necessity for spatially resolved measurements to fully understand the underlying physics of the magnon-phonon interaction. Once an external magnetic field is applied to the system, a beatting pattern with $\lambda = 22\,\mu$m is observed. We attributed this beatting pattern due to the presence of, at least, two different k-vectors on the CoFe thin film. Physically this can be attributed to the non-linear magnon dispersion relation. On the one hand we have a linear dispertion relation for phonons in case of small k-vectors, and on the other hand, non-linear magnon dispersion relation due to dynamic dipolar forces originating from the precessing magnetization.

Another observation is that the maximum BLS signal found was at the CoFe edge with LNO, in contrast with previous results on Co thin films [14], in which a continous shift in the maximum BLS signal was found.

Aditionally, a frequency sweep was performed at different positions on the sample, a surprising result was observed. At different possitions on the CoFe thin film, we get different magnetic response of the material, revealing a strong spatial magnetic dependence due to the strong presence of interferences. Thereafter, a 2-D scan of the sample at the edge of the CoFe thin film was performed with $\varphi = 35^{\text{o}}$ and $\mu_0 \text{H}_{\text{ext}} = 9.2$ mT, as exemplarily shown in Fig. 6.7.a). This value of the external magnetic field is expected to fullfill ADFMR conditions, according to previous results obtained with microwave spectroscopy. A complicated pattern was found as shown in Fig. 6.7.b), stemming for the strong influence of the standing wave present in the sample. Thereafter, we studied the magnetic response of the CoFe by placing the laser spot at the edge of the CoFe and LNO, as shown in Fig. 6.4.a), where magnon-phonon interaction was taking place with its maximum efficiency. A large magnetic response was observed close to the value at which ADFMR condition was found for VNA measurements. Thus, indicating that the FMR is indeed acoustically driven. However, a very different linewidth was found, as shown in Fig. 6.9. This difference in linewidth is attributed to the different interaction of $\mathbf{k}_{\text{SAW}}$ with $\mathbf{k}_{\text{magnon}}$ indicating that the linewidth observed in the VNA-SAW measurements is inhomogeneously broadened due to interference between SAW and spinwaves. In the BLS measurements, narrow resonance linewidthts are observed.

A FRMOKE measurement performed as shown in Fig. 6.1.a). The maximum FRMOKE signal is found at the CoFe beginning. Aditionally, a wavelength $\lambda_{\text{SAW}} = 1.33\,\mu$m is observed as expected from the IDT design for f=2.73 GHz. We observed an increase in FRMOKE signal at peaks positions inside the ADFMR condition, as previously observed on Co thin films [14]. Finally, a heat map as a function of the position on CoFe thin film and external magnetic field was measured. Showing a really interesting vertical pattern with a continous shift on maxima and minima, as observed in BLS measurements.

8 Outlook

In this thesis we have studied how SAWs can excite spin waves in CoFe thin films. Future experiments based on the findings in this work, should now investigate if the reciprocal process is also feasible. In principle and according to the reciprocity principle, it should be possible to detect SAWs launched by spin waves in a FM thin film. To this end, we present our idea of a transmutation device, as exemplarily shown in Fig. 8.1.a). This device can excite both SAWs with IDTs and, at the same time, spin-waves on a FM thin film by using a CoPlanar Waveguide (CPW).

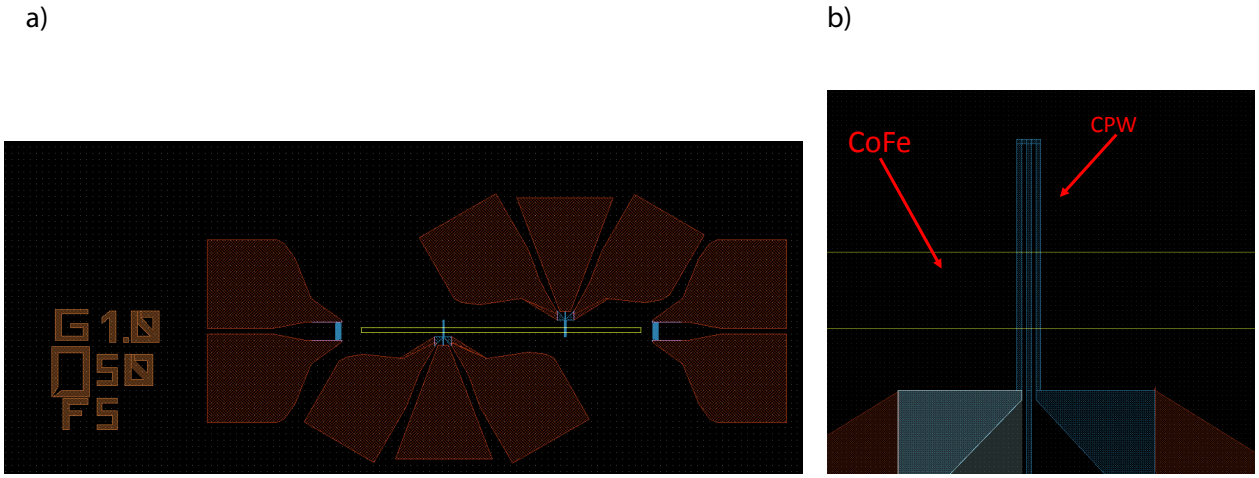

Figure 8.1: a) Transmutation device, with IDTs for SAW generation and meander antenna on top of the CoFe thin film to excite spin waves. b) Close up of the CPW located on top of the FM thin film to generate magnons.

To actually excite spin waves with k-vectors similar to the SAWs k-vectors excited by the IDTs, the choice of adequate geometry parameters for the CPW is mandatory. To this end, we follow a calculation derived from the so-called Karlqvist equations [52] which, for a single microstripe, gives the Y component of the induced rf-field, if an AC current is applied to the microstripe, which is the case considered here.

$$h_y^{\text{microstripe}}(Y) = \frac{h_0}{2w}\Theta(Y/w), \tag{8.1}$$

where $h_0 = \frac{I}{2w}$ is the current flowing through the microstripe divided by two times the width, w, of the stripe and Θ is the Heaviside step-function. The Fourier transformation of $h_y^{\text{microstripe}}(Y)$ basically gives the excitation efficiency as a function of the k-vector. This is the

simpliest case, however, with this basic explanation we can derive the excitation efficiency for more complicated structures, e.g. meander antennas. To illustrate the situation, Fig. 8.2.a) shows the AC current flowing through the antenna.

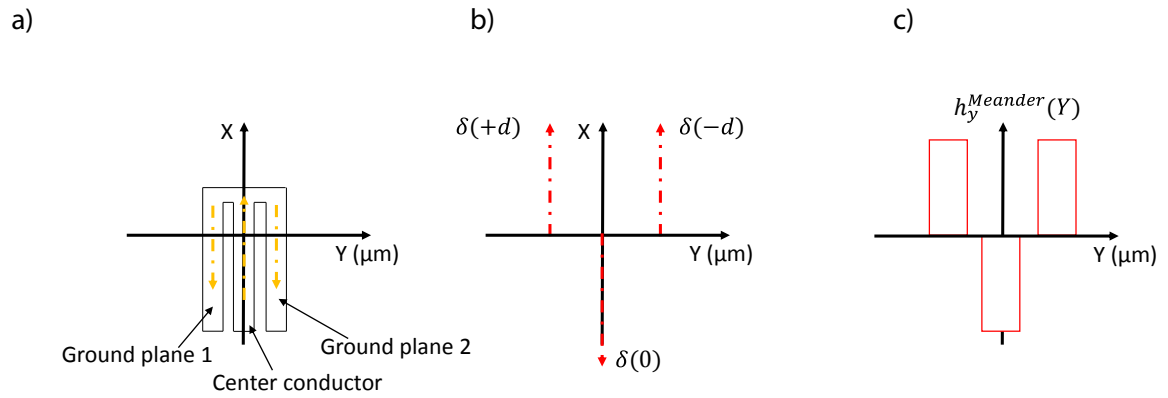

Figure 8.2: a) AC current flowing through the CPW. b) We model every microstripe as a delta function with a distance, d, between each other. c) Surface current distribution over the meander antenna. Modelled as a heaviside function at the position of every microstrip with alternating polarity.

Now, using the delta function model we can define the position of every microstripe on the CPW. The general form for the position of the 3 microstripes forming the CPW is given by

$$\mathrm{g(Y)} = [\delta(+\mathrm{d}) - \delta(0) + \delta(-\mathrm{d})] \tag{8.2}$$

where d is the distance from the center of the center conductor to the center of the ground plane, as schematically shown in Fig. 8.2.b). Now, to model the current density distribution over the meander antenna, we need to take into account that we have 3 microstripes at a distance d from each other and each microstripe is generating a rf-field given by Eq. (8.1). This mathematically is expressed by:

$$\frac{\mathrm{h_y^{CPW}(Y)}}{\mathrm{h_0}} = \mathrm{g(Y)} * \mathrm{h_y^{microstripe}(Y)}, \tag{8.3}$$

where * represent the convolution product of g and h.

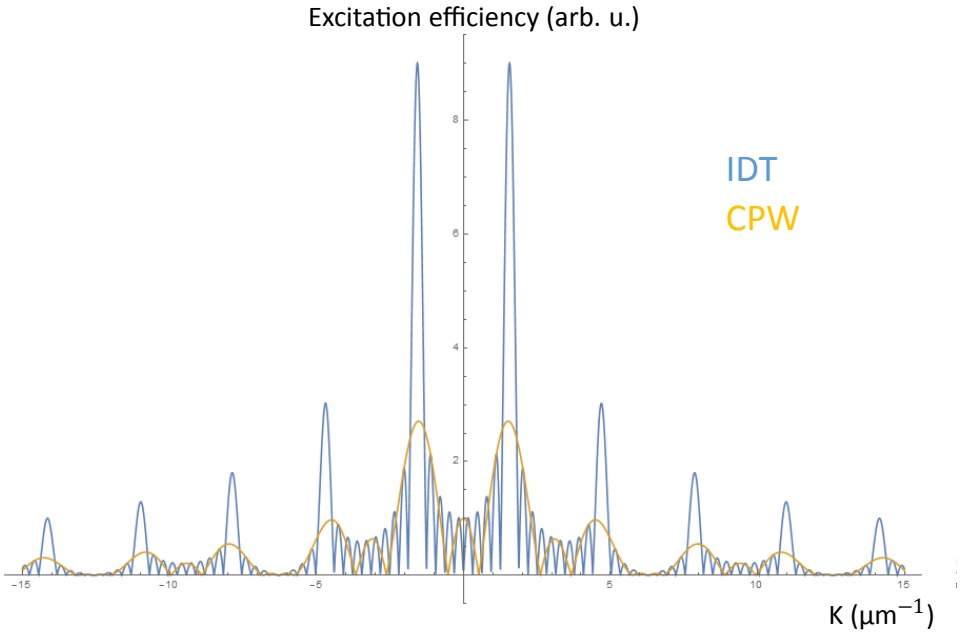

Figure 8.3: Excitation efficiency for IDT and CPW as a function of the k-vector.

Fig. 8.3 shows the excitation efficiency as a function of the k-vector calculated using this approach.. The excitation efficiency is just the Fourier transformation of the surface charge distribution of the antennae. With our IDTs we can excite SAWs with a fundamental frequency of 0.91 GHz, which corresponds to $k_{SAW} = \frac{2\pi}{\lambda} = 1.57\,\mu m^{-1}$, as shown in Fig. 8.3. With lower efficiency also higher order harmonics can be excited. With our CPW we also want to excite spin-waves on the FM thin film with roughly the same k-vectors. To do so, we carefully select the width of the center conductor w_{cc} and also the width of the ground planes, $w_{g.p.}$. The excitation efficiency in Fig. 8.3 for the meander antenna is obtained for $w_{g.p.} = w_{c.c.} = w_{gap} = 1\,\mu m$, where w_{gap} is the gap between 2 consecutive fingers. According to our simulation, the excitation efficiency when we select our configuration, thus is keeping all the parameters with the same size, is higher than when we select a center conductor with twice the width of the ground planes, as suggested in [53]. However, in our simulation we have used twice the length of the ground planes as a length for the center conductor, as exemplarily shown in Fig. 8.4.

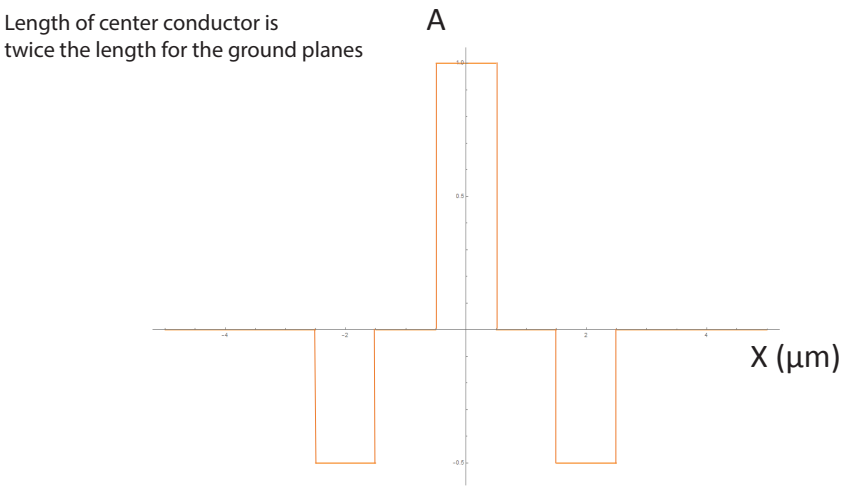

Figure 8.4: Surface charge distribution for the CPW used in our simulation.

With our transmutation device, we could determine the phonon-magnon conversion efficiency. We expect that the efficiency for generating spin waves from coherent soundwaves (and vice versa) can potentially be higher than that of generating and detecting spin waves by microwave antennas due to the overlap of coherent phonons and magnons with identical wavelength.. Another important feature is, that having established a strong interaction between phonons and magnons, we can generate a hybrid particle which has on the one hand, spin (magnon), and on the other hand, a very long propagation length (phonons). This hybrid particle with the characteristic of carrying spin and having a propagation length of several cm, which is orders of magnitude larger than the propagation length of spin-waves, would be interesting for potential magnonic devices with novel applications in data processing.

9 Appendix

In this appendix we present all the parameters used during the fabrication process of this master thesis. First, we show the parameters used for electron beam lithography. Second, the parameters used for laser writer are presented. Finally, we present all the parameters used for supettering of the diferent metals present in the samples.

9.1 Electron Beam Litography

The next tables show the spin coating parameters, the electron beam parameters and the parameters used for development. The substrates used were a 5 mm x 6xmm x 0.5 mm YZ-Cut LNO with a 0^{o} orientation black $LiNbO_3$. The original receipt is reproduced from [14].

Spin Coating
1. Applying 30 µl of PMMA/MA 33% resist layer 'AR-P 617.08' by Allresist GmbH, spin coated at 8000 rpm for 1:10 min.
2. Removing surplus PMMA on LNO backside with acetone.
3. Soft-baking on hot plate at 170°C for 2:00 min.
4. Applying 30 µl conductive resist (CR) layer 'SX AR-PC 5000/90.2' by Allresist GmbH, spin coated at 4000 rpm for 2:00 min.
5. Removing surplus CR on LNO backside with water.
6. Baking on hot plate at 90°C for 2:00 min.
7. Applying gold nanoparticles along 6 mm substrate edge for focusing.

Table 2: Table with the sping coating steps followed for electron beam lithography.

Electron Beam
Beam current: 2.7 nA
Beam voltage: 80 kV
Datum step: 7
Beam landing: vertical
Dose: 2.2 C/m^2 for patches & 2.75 C/m^2 for fingers

Table 3: Electron beam parameters used.

Development
1. Removing CR with water.
2. Development of PMMA/MA 33% with developer 'AR 600-56' holding the sample for 2:00 min in developer.
3. Removing developer by washing off with IPA for 10 s.

Table 4: Development steps followed.

9.2 Optical Lithography

The optical lithography parameters using laser writer, are presented. The substrates used were a 5 mm x 6 mm x 0.5 mm of bare LNO with their short side parallel to Z-direction, which is the main axis for SAW propagation.

Spin Coating
1. 70 μl of photoresist AZ MIR 701 is added on top of the substrate and spin coated at 5000 rmp for 60 s
2. Removing the surplus of AZ MIR 701 on LNO backside with acetone
3. Soft-baking on hot plate at 110 ^{o}C for 90 s

Table 5: Table with the sping coating steps followed for optical lithography.

Laser writer module PicoMaster 200
Dose: 50 mJ/cm^2
Attenuation: High reduction
Aperture: High resolution
Focus offset: 0 V
Red laser power: 200 µW

Table 6: Laser writer parameters used.

Development
1. Development of AZ 726 MIF with developer AZ®726MIF holding the sample for 25 s in developer.
2. Removing developer by washing off with clean water for 20 s

Table 7: Development steps followed for optical lithography.

9.3 Sputter Deposition Parameters

Sputter deposition parameters include the pressure used, power, deposition rate and time of deposition to obtain the desired thickness.

Material	Pressure (10^{-3}mbar)	Power (W)	Rate (Å/s)	Time (s)	Thickness (nm)	rpm
CoFe	0.6	30	1.9	105	20	20
Al	5	30	1.15	609	70	20
Ta	1.3	30	1	50	5	20
Pt	1.3	30	1.042	96	10	20

Table 8: Table with the sping coating steps followed for all the samples.

The Al with a thin cap of Ta to prevent oxidization was used for the IDTs and the Pt was used for the markers. The CoFe with a cap of Ta was used as a ferromagnetic material to avoid oxidization.

9.4 Sample List

The next table shows the complete sample list with all the samples used within this thesis. All these samples have been loaded with CoFe.

Name	Measurements	Remarks
AG_SAW_001 for e-beam	VNA, BLS, FRMOKE	sample used for data obtained in BLS and FRMOKE
AG_SAW_001 for laser writer	VNA	-
AG_SAW_002 for e-beam	VNA, FRMOKE	-
AG_SAW_003 for laser writer	VNA	Sample broken after removing from CPWs
AG_SAW_003 for e-beam	VNA	-
AG_SAW_004 for Laser writer	VNA	-
AG_SAW_004 for e-beam	VNA	-
AG_SAW_005_I for Laser writer	VNA	Markers are gone after lift-off
AG_SAW_005_II for Laser writer	VNA	-
AG_SAW_005_III for Laser writer	VNA	Number of finger pairs N=10, sample used to obtained data from Fig. 3.3.

Table 9: Sample list showing sample name, measurements performed and some remarks.

References

[1] J. C. Maxwell, "A dynamical theory of the electromagnetic field.," *Proceedings of the Royal Society of London*, vol. 13, pp. 531–536, 1863.

[2] J. O'neill, *Prodigal Genius, the life of Nikola Tesla.* IVES WASHBURN, INC., 1st. ed., 1944.

[3] J. Bardeen and W. H. Brattain, "The transistor, a semiconductor triode," *Phys. Rev.*, vol. 74, pp. 230–231, Jul 1948.

[4] R. R. Schaller, "Moore's law: past, present and future," *IEEE Spectrum*, vol. 34, pp. 52–59, June 1997.

[5] F. T. Ulaby, "The legacy of moore's law," *Proceedings of the IEEE*, vol. 94, pp. 1251–1252, July 2006.

[6] W. Gerlach and O. Stern, "Der experimentelle nachweis der richtungsquantelung im magnetfeld," *Zeitschrift für Physik*, vol. 9, pp. 349–352, Dec 1922.

[7] S. Bhatti, R. Sbiaa, A. Hirohata, H. Ohno, S. Fukami, and S. Piramanayagam, "Spintronics based random access memory: a review," *Materials Today*, vol. 20, no. 9, pp. 530 – 548, 2017.

[8] L. Liensberger, L. Flacke, D. Rogerson, M. Althammer, R. Gross, and M. Weiler, "Spin-wave propagation in metallic cofe films determined by microfocused frequency-resolved magneto-optic kerr effect," *IEEE Magnetics Letters*, vol. 10, 2019.

[9] M. Weiler, *Magnon-Phonon interactions in ferromagnetic thin films.* PhD thesis, 2012.

[10] M. Weiler, H. Huebl, F. S. Goerg, F. Czeschka, R. Gross, and T. Goennewein, "Spin pumping with coherent elastic waves," *Physical Review Letters*, vol. 108, no. 176601, 2012.

[11] L. Dreher, M. Weiler, M. Pernpeintner, H. Huebl, R. Gross, M. Brandt, and S. Goennenwein, "Surface acoustic wave driven ferromagnetic resonance in nickel thin films: Theory and experiment," *Physical review B*, vol. 86, no. 134415, 2012.

[12] D. Schwienbacher, M. Pernpeintner, L. Liensberger, E. R. J. Edwards, H. T. Nembach, J. M. Shaw, M. Weiler, R. Gross, and H. Huebl, "Magnetoelasticity of co25fe75 thin films," *Journal of Applied Physics*, vol. 126, no. 10, 2019.

[13] L. Flacke, L. Liensberger, M. Althammer, H. Huebl, S. GeprÃ€gs, K. Schultheiss, A. Buzdakov, T. Hula, H. Schultheiss, E. R. J. Edwards, H. T. Nembach, J. M. Shaw, R. Gross, and M. Weiler, "High spin-wave propagation length consistent with low damping in a metallic ferromagnet," *Applied Physics Letters*, vol. 115, no. 12, p. 122402, 2019.

[14] M. Muehlenhoff, "Microwave frequency magnetoacoustic interactions in ferromagnetic thin films," Master's thesis, 2017.

[15] M. A. W. Schoen, D. Thonig, and J. Shaw, "Ultra-low magnetic damping of a metallic ferromagnet," *Nat. Phys.*, vol. 12, no. 839, 2016.

[16] R. Wiegert and M. Levy, "Correlation between high-frequency rayleigh wave attenuation and dc magnetoresistance in nickel thin films," *Journal of Applied Physics*, vol. 61, no. 4270, 1987.

[17] R. Wiegert, "Magnetoelastic surface acoustic wave attenuation and anisotropic magnetoresistance in ni3fe thin films," *Journal of applied physics*, vol. 91, no. 10, 2002.

[18] S. Blundell, *Magnetism in Condensed Matter*. 2001.

[19] M. C. Hickey and J. S. Moodera, "Origin of intrinsic gilbert damping," *Phys. Rev. Lett.*, vol. 102, p. 137601, Mar 2009.

[20] L. Landau and E. Lifshits, "On the theory of the dispersion of magnetic permeability in ferromagnetic bodies," *Phys. Zeitsch. der Sow*, vol. 8, pp. 153–169, 1935.

[21] T. L. Gilbert, "A phenomenological theory of damping in ferromagnetic materials," *IEEE Transactions on Magnetics*, vol. 40, pp. 3443–3449, 2004.

[22] L. Liensberger, "Spin-orbit torques and magnetization dynamics in non-collinear magnets," Master's thesis, 2017.

[23] Rayleigh, "On waves propagated along the plane surface of an elastic solid," pp. 4–11, 1885.

[24] X. Chen, M. A. Mohammad, J. Conway, B. Liu, Y. Yang, and T. ling Ren, "High performance lithium niobate surface acoustic wave transducers in the 4-12 ghz super high frequency range," *Journal of Vacuum Science and Technology*, vol. 33, 2015.

[25] W. R. Smith, H. M. Gerard, and W. Jones, "Analysis and design of dispersive interdigital surface-wave transducers," *IEEE transactions on microwave theory and techniques*, vol. 20, no. 7, pp. 458–471, 1972.

[26] R. S. Weis and T. Gaylord, "Lithium niobate: Summary of physical properties and crystal structure," *Appl. Phys. A solids and surfaces*, vol. 37, no. 4, pp. 191–203, 1985.

[27] D. P. Morgan, "Surface-wave devices for signal processing," 1991.

[28] M. Pernpeitner, "Magnon-phonon coupling in ferromagnetic thin films," 2012.

[29] R. Gross and A. Marx, *Festkoerperphysik*. 2012.

[30] S. Chikazumi, *physics of Ferromagnetism*. 2nd ed., 1997.

[31] M. Hiebel, *Fundamental of vector network analysis*. 7 ed., 2016.

[32] E. Hewitt and R. E. Hewitt, "The gibbs-wilbraham phenomenon: An episode in fourier analysis," *Archive for History of Exact Sciences*, vol. 21, pp. 129–160, Jun 1979.

[33] T. Butz, *Fourieretransformation fuer Fussgaenger*. 6 ed., 2009.

[34] C. Heeg, "Spin mechanics at radio frequencies," Master's thesis, 2010.

[35] L. Brillouin, "Diffusion de la lumiere et des rayons x par un corps transparent homogene," *Ann. Phys*, vol. 9, no. 88, 1922.

[36] T. Sebastian, K. Schultheiss, B. Obry, B. Hillebrands, and H. Schultheiss, "Micro-focused brillouin light scattering: Imaging spinwaves at the nanoscale," *Frontiers in Physics*, vol. 3, 06 2015.

[37] J. G. Dil, J. A. van Hijningen, F. van Dorst, and R. M. Aarts, "Tandem multipass fabry-perot interferometer for brillouin scattering," *Applied Optics*, vol. 20, no. 8, 1981.

[38] L. Flacke, "Spin-pumping and spin wave damping in co25fe75 thin-film heterostructures," Master's thesis, 2018.

[39] H.-J. J. Liu, *Brillouin Light Scattering Study of Linear and Nonlinear Spin Waves in Continuous and Patterned Magnetic Thin Films*. PhD thesis, 2014.

[40] W. Demtroeder, *Elektrititaet und Optik*, vol. 4. 2006.

[41] S. Datta, "Surface acoustic wave devices," 1986.

[42] MicroChemicals, "Baking steps in photoresists processing," 2013.

[43] S. Datta, "Surface acoustic wave devices," 1986.

[44] A. J. Slobodnik, "Surface acoustic waves and saw materials," *Proceedings of the IEEE*, vol. 64, pp. 581–595, May 1976.

[45] C. Campbell, *Surface Acoustic Wave Deviced and Their Signal Processing Applications*. 1st ed., 1989.

[46] H. E. Engan, "Excitation of elastic surface waves by spatial harmonics of interdigital transducers," 1969.

[47] H. Soede, "Surface acoustic waves at ferromagnetic piezoelectric interfaces," Master's thesis, 2009.

[48] C. L. Platt, A. E. Berkowitz, D. J. Smith, and M. R. McCartney, "Correlation of coercivity and microstructure of thin cofe films," *Journal of Applied Physics*, vol. 88, no. 4, pp. 2058–2062, 2000.

[49] E. Stoner and E. Wohlfarth *Phil. Trans. R. Soc*, vol. 240, no. 599, 1948.

[50] D. Labanowski, A. Jung, and S. Salahuddin, "Power absorption in acoustically driven ferromagnetic resonance," *Applied Physics Letters*, vol. 108, no. 2, p. 022905, 2016.

[51] J. Stigloher, M. Decker, H. S. Körner, K. Tanabe, T. Moriyama, T. Taniguchi, H. Hata, M. Madami, G. Gubbiotti, K. Kobayashi, T. Ono, and C. H. Back, "Snell's law for spin waves," *Phys. Rev. Lett.*, vol. 117, p. 037204, Jul 2016.

[52] O. Karlqvist, "Calculation of the magnetic field in the ferromagnetic layer of a magnetic drum," 1954.

[53] V. Vlaminck and M. Bailleul, "Spin-wave transduction at the submicrometer scale: Experiment and modeling," *Phys. Rev. B*, vol. 81, p. 014425, Jan 2010.

Acknowledgment

Over the last 13 months there were many people who contributed in many ways to this work. Without the help, support, knoweledge and good advices of most of them it will be impossible to finish this work. I really would like to thank:

Prof. Dr. Rudolf Gross, for offering me the possibility to realize my master thesis at the Walther-Meißner Institut and supporting us as students.

Dr. Mathias Weiler, my advisor and the person who motivated me. Your magnetism lectures catched my attention and interest, and inspired me to expand my knoweledge in this interesting and promising field. I'm so thankful for all the discussion about the physics and also how to develop my work and go for the next step. I would also like to thank you for the opportunity to work at the Walther-Meissner-Institut as a working student during the summer semester 2018. It was a nice experecience.

Dr. Mathias Althammer, for his advice regarding fabrication with the SUPERBOWL and also to expend the necessary time helping me with the new bonding machine when I really needed.

Luis Flacke and Lukas Liensberger, for helping me and advising me with everything I needed. From sample fabrication to BLS and FRMOKE setups, your guidance helped me a lot to get a real understanding of the set ups and the physics behind.

Daniel Schwienbacher, for his help around the e-Beam.

To all the guys in the room 108, for making our office a nice space to work. For making me feel like home. A nice enviroment is always necessary to reach the final goal.

Manuel Müller, for his invaluable help with everything. PC configuration, physics, guidance with VNA measurements and of course for being a nice guy and someone I can call friend. Without you this year would have been more complicated.

The workshop crew, for helping me to find the suitable screws for my sample holder and also for fixing all the issues I experienced in the clean room.

To my family, Loli and Jaime, my parents, and Elena, my sister, for being my personal support. For always helping me and make my decissions much easier to carry. I'm so proud and thankful for the family we are.

To my "Deutsche Familie": Antonio, Leles, Sampe, Cristina, Marc and the rest of the guys. For always have a nice plans for the weekends and for make me feel like home even at 3000 km far away from it.

Specially thanks to my girlfriend, Nuria. For sharing this way with me from the beginning. For making the decission to come to Germany with you, the adventure of my life. For always have open ears for me after a bad day, and of course, for helping me with everything I needed. Without you this would have been impossible.